# Linking 3D long-term slow-slip cycle models with rupture dynamics: the nucleation of the 2014 Mw 7.3 Guerrero, Mexico earthquake

**Duo Li**[1],**Alice-Agnes Gabriel**[2,1]

[1]Department of Earth and Environmental Sciences, Ludwig-Maximilians-Universität München, Munich, Germany

[2]Institute of Geophysics and Planetary Physics, Scripps Institution of Oceanography, University of California San Diego, La Jolla, USA

**Key Points:**

- We present the first 3D linked models of dynamic earthquake rupture and long-term slow slip cycles along the flat-slab Cocos plate
- The modeled slow slip cycles and earthquake dynamic rupture capture key observations on timescales from decades to seconds
- The crucial transient stress evolution of the long-term slow slip cycles may have initiated the 2014 $M_{\mathrm{w}}$7.3 Guerrero earthquake

Corresponding author: D. Li, dli@geophysik.uni-muenchen.de

**Abstract**

Slow slip events (SSEs) have been observed in spatial and temporal proximity to megathrust earthquakes in various subduction zones, including the 2014 $M_w$7.3 Guerrero, Mexico earthquake which was preceded by a $M_w$ 7.6 SSE. However, the underlying physics connecting SSEs to earthquakes remains elusive. Here, we link 3D slow-slip cycle models with dynamic rupture simulations across the geometrically complex flat-slab Cocos plate boundary. Our physics-based models reproduce key regional geodetic and teleseismic fault slip observations on timescales from decades to seconds. We find that accelerating SSE fronts transiently increase shear stress at the down-dip end of the seismogenic zone, modulated by the complex geometry beneath the Guerrero segment. The shear stresses cast by the migrating fronts of the 2014 $M_w$ 7.6 SSE are significantly larger than those during the three previous episodic SSEs that occurred along the same portion of the megathrust. We show that the transient stresses caused by this SSE are large enough to nucleate earthquake dynamic rupture. However, additional frictional asperities in the seismogenic part of the megathrust are required to explain the observed complexities in the coseismic energy release and static surface displacements of the 2014 $M_w$7.3 Guerrero earthquake. We conclude that it is crucial to jointly analyze the long- and short-term interactions and complexities of SSEs and megathrust earthquakes across several (a)seismic cycles accounting for megathrust geometry. Our study has important implications for identifying earthquake precursors and understanding the link between transient and sudden megathrust faulting processes.

## Plain Language Summary

The 2014 Mw 7.3 Guerrero, Mexico earthquake was preceded by an Mw 7.6 slow slip event, a transient of aseismic fault slip, which offers a valuable opportunity to explore the relationship between slow slip and major subduction earthquakes. By modeling both long-term cycles of slow slip events (SSEs) and dynamic earthquake rupture, we reproduce various measurements from geodetic surveys and seismic recordings. We find that as the migrating front of the 2014 SSE accelerated, it caused a temporary increase in shear stress at the depth of 22 km on the fault where the earthquake occurred. In this case, the stress levels of the preceding 2014 Mw 7.6 slow slip were notably higher than previous SSEs which appeared in the same fault portion between 2001 and 2014, and may have contributed to initiating the earthquake. Additionally, we found that variations in friction on the fault surface affect the complexity of energy release and surface displacements during the earthquake. By examining the temporary and long-term interactions between SSEs and earthquakes, we gain important insights into potential earthquake precursors and the processes involved

in how faults move. This research holds significant implications for enhancing our understanding of how large earthquakes occur in subduction zones.

## 1 Introduction

Transient quasi-static fault deformation, slow-slip events (SSEs), or silent earthquakes have been observed at convergent plate boundaries (Dragert et al., 2001; Shelly et al., 2006; Douglas et al., 2005; Schwartz & Rokosky, 2007; Peng & Gomberg, 2010) and at large continental faults, e.g., the San Andreas fault (Linde et al., 1996; Rousset et al., 2019). SSEs may be accompanied by low-frequency seismic radiation, including non-volcanic tremors (NVTs), low-frequency earthquakes (LFEs), and very-low-frequency earthquakes (VLFEs) (Shelly et al., 2007; Khoshmanesh et al., 2020). SSEs usually slip 10-100 times faster than the tectonic loading and last from days to years at depths close to the brittle-ductile transition (Dragert et al., 2001; Schwartz & Rokosky, 2007; Peng & Gomberg, 2010). The physical mechanisms underlying SSEs and their interaction with earthquakes are debated (Bürgmann, 2018): The spatial viability of both fast and slow earthquakes on plate-boundary faults has been attributed to several factors, including structural and material heterogeneity (Tobin & Saffer, 2009; Wang, 2010; Lay et al., 2012; Li & Liu, 2016; Ulrich et al., 2022), rheological variability with depth (Gao & Wang, 2017; Saffer & Wallace, 2015) and fluid migration within oceanic sedimentary layers (W. B. Frank et al., 2015; Zhu et al., 2020).

The kinematic migration patterns of off-shore aseismic slip are often challenging to constrain due to the lack of dense geodetic observations. Sequences of foreshocks and migrating seismicity before large events such as the 2011 Tohoku-Oki earthquake have been interpreted as proxies for aseismic fault slip and as potential long-term precursory signals of megathrust earthquake nucleation processes (A. Kato et al., 2012). Other observations of possible precursory signals include the acceleration of a $M_{\mathrm{w}}$ 6.5 slow slip event that was recorded by the land-based GPS stations eight months before the 2014 $M_{\mathrm{w}}$ 8.1 North Chile earthquake (Socquet et al., 2017a).

Whether transient slow slip can serve as a universal precursor of eminent megathrust earthquake initiation is essential for seismic and tsunami hazard assessments in metropolitan margins (Ruiz et al., 2014; Obara & Kato, 2016; Pritchard et al., 2020; Bürgmann, 2018). However, the spatial and temporal interactions between slow and fast earthquakes, specifically the potential of slow-slip triggering megathrust earthquakes, remain enigmatic. Due to the observational challenges associated with the large variability of space and time scales, physics-based models are indispensable to illu-

minate the physics and in-situ fault properties rendering SSE triggering of large earthquakes plausible.

On April 18, 2014, a $M_w$ 7.3 megathrust earthquake struck the coast of Mexico at the western edge of the Guerrero Gap, which had experienced no significant seismic events since 1911(Kostoglodov et al., 1996; Radiguet et al., 2012). Geodetic inversions suggest that long-term slow-slip cycles have accommodated most of the plate convergence on the sub-horizontal oceanic slab between 20-45 km depth in Guerrero (Kostoglodov et al., 1996; Radiguet et al., 2012, 2016) (Figure 1a). In addition to long-term SSEs, transient bursts of short-term low-frequency earthquakes and non-volcanic tremors have been detected at different depths along the slab (Pérez-Campos et al., 2008; Husker et al., 2012; W. B. Frank et al., 2015; W. Frank et al., 2015). Slow-slip and slow earthquakes have been attributed to the elevated pore fluid pressure associated with an ultra-low velocity layer atop the subducting plate derived from dense-array seismic imaging(Song et al., 2009). Recent off-shore seismic observations have revealed a combination of earthquakes, aseismic and creeping deformation, suggesting the existence of multiple asperities across the slab interface (Plata-Martinez et al., 2021). Considering the unique slip characteristics of the Guerrero Gap, the initiation of the 2014 $M_w$7.3 earthquake has been related to the accumulated static Coulomb stress changes cast by an ongoing slow-slip event below 20 km depth that eventually accumulated an equivalent moment magnitude of $M_w$7.6 on the megathrust interface (Radiguet et al., 2016; Gualandi et al., 2017a).

In this study, we present 3D numerical models of the dynamic rupture of the 2014 $M_w$7.3 Guerrero earthquake, linked to 3D episodic slow-slip cycles under long-term tectonic loading, ensuring consistent stress states across the fault interface. Physics-based models of earthquake initiation, propagation, and arrest require choices regarding the pre-existing state of stress and fault strength governing frictional sliding (Oglesby & Mai, 2012; Gabriel et al., 2012; van Zelst et al., 2019; Harris et al., 2021; Ramos et al., 2021; Tinti et al., 2021). Our SSE cycle and dynamic rupture models account for the same geophysical and geological observational inferences, such as the regional slab geometry, elevated pore fluid pressure, and depth-dependent frictional strength constrained from laboratory experiments and thermal modeling (Section 2). We bridge time scales from decades governing four episodes of long-term SSEs to fractions of seconds during earthquake rupture within the Guerrero Gap using the SSE cycle results to inform the dynamic earthquake rupture scenario models. The modeled, observationally constrained, transient stress evolution of the 2014 SSE event can lead to spontaneous co-seismic failure in the hypocentral region of the Guerrero earthquake. However, the episodic increase in shear stress caused by the three preceding SSEs, which correspond to the 2002, 2006, and 2009-2010 SSEs, remains too small compared to the high static fault strength

required to match observations in the dynamic rupture model (Section 3). We also find that, in addition to SSE-induced stress heterogeneity, the complex propagation and arrest of the Guerrero earthquake require pre-existing variable friction properties. Our study provides a mechanically self-consistent model for slow-slip triggered megathrust earthquakes and has important implications for the interaction between earthquakes and slow-slip in subduction zones and at large continental faults worldwide (Section 4).

## 2 Methods

### 2.1 3D quasi-dynamic simulations of the long-term slow-slip cycles

Direct observations of slow-slip cycles are limited, motivating numerical simulations to elucidate the underlying mechanics of SSE and earthquake interactions. We simulate long-term slow-slip sequences on a convergent plate boundary and analyze the time-dependent evolution of slip rates and shear stresses on the fault interface in 3D (Figure 1b). We use a quasi-dynamic formulation and the Boundary Element Method (BEM). Our forward model adopts a laboratory-derived rate-and-state friction law and a 3D realistic subducting slab geometry beneath central Mexico. The governing equations relate the temporal shear stress evolution of an individual element in response to fault slip and long-term plate convergence following Rice (Rice, 1993) as

$$\tau_i\left(t\right) = -\sum_{j=1}^{N} K_{i,j}\left(\delta_j\left(t\right) - V_{pl}t\right) - \eta\frac{d\delta_i\left(t\right)}{dt}, \tag{1}$$

where $\delta_i\left(t\right)$ is the fault slip and $K_{i,j}$ is the shear stress in element $j$ due to a unit dislocation in dip direction of element $i$. The static Green's function $K_{i,j}$ is calculated using triangular dislocations in a uniform half-space (Stuart et al., 1997) assuming a homogeneous shear modulus of $\mu =$ 30 GPa and density $\rho = 2670kg/m^3$. The plate convergent rate $V_{pl}$ is set to be uniformly 61 mm/year based on a global plate motion model, the PVEL model (DeMets et al., 2010).

We use the open-source code TriBIE (`https://github.com/daisy20170101/TriBIE`) (Li & Liu, 2016; Perez-Silva et al., 2021), which is parallelized with OpenMPI and has been verified in 2D and 3D community benchmark exercises (Jiang et al., 2022; Erickson et al., 2023). We here use the quasi-dynamic approach approximating inertia effects with radiation damping for our SSE cycle simulations. To this end, the radiation damping factor $\eta = \mu/(2c_s)$ (with $c_s$ being the shear wave speed) has been introduced (Rice, 1993). Compared to fully dynamic simulations, the quasi-dynamic approach can lead to similar overall seismic cycle behavior but differing rupture dynamics (Lapusta

& Liu, 2009; Thomas et al., 2014; Jiang et al., 2022). We detail all slow-slip cycle modeling parameters in the following.

### *2.1.1 Effective normal stress*

Figure 2b shows the along-depth profiles of our assumed effective normal stress $\bar{\sigma}_n$, pore fluid pressure ($p_f$), hydrostatic ($0.37^*\sigma_z$) and lithostatic pressures ($\sigma_z$). We assume that lithostatic pressure is depth-dependent with a constant overburden gradient (i.e., $\sigma_z = \rho g(-z)$). The effective normal stress, defined as the difference between lithostatic pressure and pore fluid pressure, increases with depth at a constant gradient $\bar{\sigma}_n = 28$ MPa/km until a depth of 2.7 km. At lower depths, effective normal stress remains constant as $\bar{\sigma}_n = 50$ MPa except at the SSE source depth between 20 and 45 km. An effective normal stress of 50 MPa at seismogenic depth is a common assumption used in community benchmark studies (Jiang et al., 2022).

To reproduce the relatively low stress drops inferred for SSEs, we assume a low effective normal stress of $\bar{\sigma}_n^{SSE} = 2.5$ MPa at depths between 20 km and 45 km based on our previous work for a narrower slab geometry (Perez-Silva et al., 2021) and linked to elevated pore fluid pressure. Such high, near-lithostatic pore fluid pressure is supported by the observed elevated ratio between $V_p$ and $V_s$ from seismic imaging along the coast of southwest Japan, Cascadia, and central Mexico (Audet & Burgmann, 2014; Song et al., 2009).

### *2.1.2 Rate-and-state friction*

Fault shear strength in the quasi-dynamic SSE simulation is governed by a laboratory-derived rate and state-dependent friction law, the aging law (Dieterich, 1979; Ruina, 1983). The effective friction coefficient $f$ depends on the fault slip rate $v$ and a single state variable $\theta$ as

$$\tau = \bar{\sigma}_n f = (\sigma_n - p)\left[f_0 + a\ln\left(\frac{v}{v_0}\right) + b\ln\left(\frac{v_0\theta}{D_{RS}}\right)\right]. \tag{2}$$

Here, $a$ and $b$ are non-dimensional friction parameters for the direct effect and evolution effect, respectively, $D_{RS}$ is the characteristic slip distance over which $\theta$ evolves in response to velocity steps, $f_0$ is the friction coefficient at a reference velocity $v_0$ at steady state, and $\bar{\sigma}_n = \sigma_n - p_f$ is the effective normal stress, defined as lithostatic loading stress minus the pore fluid pressure.

At steady state $\theta = D_{RS}/v$, the friction coefficient is $f_{ss} = f_0 + (a-b)\ln(\frac{v}{v_0})$. Slip remains stable, and any slip perturbation evolves toward a steady state when the friction stability param-

eter $(a-b)$ is positive (velocity-strengthening, VS). Slip can be either unstable or conditionally stable when $(a-b)$ is negative (velocity-weakening, VW). We use uniform distributions for the initial slip rate $V_{ini}$ and the initial state variable $\theta_{ini}$ on the entire fault.

We adopt the definition of the critical nucleation length $h^*_{RA}$ based on the fracture energy balance for a quasi-statically expanding crack (Rubin & Ampuero, 2005),

$$h^*_{RA} = \frac{2\mu b D_{RS}}{\pi(1-\nu)(b-a)^2\bar{\sigma}}. \tag{3}$$

Here, we assume a shear modulus of $\mu = 30$ GPa and Poisson's ratio of $\nu = 0.25$. The ratio between the maximum width of the velocity-weakening portion of the slab and the critical nucleation length $(h^*_{RA})$ significantly affects the slip behavior of modeled SSEs (Lapusta & Liu, 2009; Liu & Rice, 2009) (Li & Liu, 2017; Perez-Silva et al., 2021).

For faults governed by rate-and-state friction, the quasi-static process zone at a non-zero rupture speed can be estimated as $\Lambda_0 = C\frac{\mu^* D_{RS}}{b\sigma_n}$, where $C$ is a constant of order 1(Day et al., 2005; Lapusta & Liu, 2009; Jiang et al., 2022), $\mu^* = \mu$ for antiplane strain and $\mu^* = \mu/(1-\nu)$ for plane strain, where $\nu$ is Poisson's ratio. We note that our mesh size is considerably smaller than $\Lambda_0$ which ensures numerical stability and accuracy.

We adopt the empirical "aging" law that can be interpreted to account for time-dependent healing of microscopic stationary frictional contacts (Beeler et al., 1996, e.g.,), for describing the temporal evolution of state variable $(\theta)$:

$$\frac{d\theta}{dt} = 1 - \frac{V\theta}{D_{RS}}. \tag{4}$$

To regularize the solution at low slip rates we use the modification proposed by Rice(Rice & Ben-Zion, 1996):

$$\mu = asinh^{-1}[\frac{V}{2v_0}exp(\frac{\mu_0 + b\ln(v_0\theta/D_{RS})}{a})], \tag{5}$$

which is Eq. 2 when $V >> 0$.

A distribution of $(a-b)$ at different temperatures has been obtained from laboratory experiments for wet gabbro gouges (He et al., 2007). We project this temperature-dependent $(a-b)$ distribution onto the slab interface using the thermal profile from a 2D steady-state thermal model constrained by P-wave seismic tomography in central Mexico (Manea & Manea, 2011). We assume a downdip transition temperature, $(a-b) = 0$, of 415$^o$C, which coincides with the maximum downdip extent of long-term SSEs inferred from GPS inversions(Radiguet et al., 2012). Velocity-strengthening

conditions $(a-b) > 0$ are imposed at the two lateral sides of the model domain to stabilize slip towards the plate convergence rate. The distribution of $(a-b)$ across the entire slab is shown in Figure 2a. The physical parameters including friction, initial stress, and elastic material properties aforementioned are listed in Table 1.

### 2.2 3D SSE-initiated dynamic rupture models for the Guerrero earthquake

We use the open-source software *SeisSol* (https://github.com/SeisSol), which is based on the Arbitrary High-order Derivative (ADER) Discontinuous Galerkin (DG) finite element method, to perform simulations of earthquake rupture dynamics and seismic wave propagation (Käser & Dumbser, 2006; Dumbser & Käser, 2006; Pelties et al., 2012). *SeisSol* has been optimized for modern high-performance computing architectures including an efficient local time-stepping algorithm (Breuer et al., 2014; Heinecke et al., 2014; Uphoff et al., 2017; Krenz et al., 2021) and has been validated against several community benchmarks following the SCEC/USGS Dynamic Rupture Code Verification exercises (Pelties et al., 2014; Harris et al., 2018). Stress and particle velocities are approximated with 3rd-degree polynomials, yielding 4th-order accuracy in space and time during wave propagation simulation. We detail all dynamic rupture modeling parameters in the following.

#### *2.2.1 Dynamic rupture initial stresses*

We constrain the initial stresses in the dynamic rupture model from a snapshot of the shear and effective normal stresses across the fault interface in the 2014 SSE model. We track the traction ratio as the slow-slip fronts migrate along-strike and find that the local peak in the hypocentral region appears on day 317 (Figures 3f and 4a ). This local peak of traction ratio is associated with the acceleration of the migrating front from 0.5 km/day to 3 km/day (Figures 4b,c). The shear traction and effective normal stress on day 317 of the 2014 SSE quasi-dynamic model are saved and spatially interpolated onto the higher-resolution dynamic rupture mesh of the subduction fault surface using the package ASAGI (Rettenberger et al., 2016). The resulting ratio between the initial shear and effective normal stress is shown in Figures 3f. The time-dependent evolution of the traction ratio parameter on the fault during the modeled SSE is shown in Movie S2.

#### *2.2.2 Velocity structure*

We use a 1D depth-dependent model of the density and seismic velocities to set the elastic properties ($\mu$ and $\lambda$) in the dynamic rupture model, as shown in Figures S5 and 1b. This 1D velocity

model is based on seismic imaging of the central Mexico subduction zone (Dougherty & Clayton, 2014) using the Mapping the Rivera Subduction Zone (MARS) seismic array, which consists of 50 broadband seismic instruments with a station spacing of ∼40 km deployed from January 2006 to June 2007. This 1D layered velocity structure captures the major features of the subsurface (Song et al., 2009; Kim et al., 2010).

#### *2.2.3 Linear slip-weakening friction*

In the dynamic rupture simulations, we adopt a linear slip-weakening (LSW) friction law to constrain the fault frictional strength which has been shown to largely depend on the fault slip distance in laboratory experiments (Ida, 1972; Palmer & Rice, 1973). LSW friction laws have been widely used in dynamic rupture simulations including models of large megathrust earthquakes such as the 2004 $M_w$ 9.1-9.3 Sumatra–Andaman earthquake (Uphoff et al., 2017; Ulrich et al., 2022), 2011 $M_w$ 9.0 Tohoku-Oki earthquake (Galvez et al., 2014), and rupture scenarios for the Cascadia subduction zone (Ramos et al., 2021).

The LSW friction law is parameterized by the static ($\mu_s$) and dynamic ($\mu_d$) friction coefficients, critical slip-weakening distance ($d_c$), and frictional cohesion $c_0$. These initial conditions are difficult to constrain on the scale of megathrust slip but play an important role in dynamic rupture nucleation and propagation (van Zelst et al., 2019; Ulrich et al., 2022). Based on several trial dynamic rupture scenarios we set the static friction coefficient to $\mu_s$=0.626 and the dynamic friction coefficient to $\mu_d$=0.546 within the assigned rupture asperities which yield realistic co-seismic rupture dynamics and arrest as well as spontaneous nucleation at a depth of 22 km due to the 2014 SSE stressing. Our choice of static friction allows for a smooth nucleation process at the hypocenter without introducing additional overstress and is within the range of effective static friction typically used in dynamic rupture megathrust scenarios (Galvez et al., 2014; Ramos & Huang, 2019; Madden et al., 2022).

In our preferred model (referred to as Model A1), we include two asperities. We use a constant $\mu_d$ within each asperity. An increase in $\mu_d$ outside the asperities is required for smooth and spontaneous rupture arrest. We increase $\mu_d$ outside the asperities using an exponential function in space $G_1(r_1, r_2)$:

$$G_1(r_1, r_2) = \begin{cases} min(1.0, \frac{1}{0.75} min(0.75, \exp(\frac{r_1^2}{r_1^2 - r_{c1}^2})) + \frac{1}{0.75} min(0.75, \exp(\frac{r_2^2}{r_2^2 - r_{c2}^2})) \; r_1 \leq r_{c1}, r_2 \leq r_{c2} \\ 0.0 \; otherwise \end{cases} \tag{6}$$

where $r_i$ is defined as the epicentral distance from the center of each asperity $r_i = \sqrt{(x - x_{0i})^2 + (y - y_{0i})^2}, i = 1, 2$. The radii of both asperities $r_{c1}, r_{c2}$, are chosen as 38 km and 42 km, respectively. The locations of their centers ($x_{0i}$ and $y_{0i}$) are listed in Supplementary Table S2, and the distribution of $G_1$ is shown in Figure S7.

We find that by increasing $\mu_d$ to values 30% ($\mu_d = 0.826$) higher than $\mu_s$, dynamic rupture gradually stops at the edges of the asperities. This setup results in a comparable duration and peak of moment release to teleseismic inversion (Ye et al., 2016) (Figure 6a). The on-fault distribution of $\mu_d$ following $0.826 - 0.28 \times G_1(r_1, r_2)$ is shown in Figure 6f.

The critical slip distance $d_c$ is generally not well constrained by seismic observations, for example, because of strong trade-offs with the assumed yield strength (Guatteri & Spudich, 2000), limited near-field strong ground motion observations (Mikumo et al., 2003), and fault zone heterogeneity(Galvez et al., 2014; Collettini et al., 2019; Gallovic et al., 2019). The choice of $d_c$ also determines critical nucleation size and the required numerical on-fault resolution constrained by the process zone width (Day et al., 2005; Wollherr et al., 2018). Here, we use a relatively small and uniform critical slip-weakening distance of $d_c$=0.05 m which leads to realistic final slip, seismic stress drop, moment, and time-dependent moment release of the SSE-initiated dynamic rupture scenarios. We choose this slip-weakening critical distance since it allows for SSE-initiated large earthquake rupture and is at the lower limit of estimates from seismological observations (Mikumo et al., 2003) and at the upper limit of laboratory inferred estimates ($10^{-5} - 10^{-3}$ m) (Marone, 1998). In an alternative model using $d_c$ =0.5 m (not shown), dynamic rupture arrests quickly after the nucleation phase (Supplementary Information Text S2; FigureS12).

It is difficult to observationally constrain the frictional cohesion $c_0$ of natural faults. In dynamic simulations, $c_0$ is typically assumed as 0.4 - 1.0 MPa at seismogenic depths and as high as 4-8 MPa at shallow depths to prevent large shallow slip or localized near-surface super-shear rupture speeds (Ramos & Huang, 2019; Wollherr et al., 2019). Here, we set $c_0 = 1.0$ MPa at depths shallower than 6.5 km and linearly decrease $c_0$ to 0 MPa at a depth of 10 km. All linear slip-weakening friction parameters ($\mu_s, \mu_d, d_c, c_0$) are listed in Table 2.

### 2.3 Fracture energy and stress drop

Fracture energy, defined as the strain energy consumed during shear sliding in the framework of linear elastic fracture mechanics, has been closely linked to fault-weakening mechanisms (Abercrombie & Rice, 2005; Tinti et al., 2005). In dynamic rupture simulations governed by linear slip-weakening friction, we can calculate fracture energy as follows:

$$G_c = \frac{(\tau_y - \tau_d)d_c}{2}, \tag{7}$$

where $G_c$ is the fracture energy, $\tau_y$ denotes the frictional yielding strength, and $\tau_d$ is the dynamic residual shear stress at a specific location on the fault.

We estimate the average fracture energy during the initial stage of dynamic rupture $E_{nu}$ using :

$$\bar{G}_{nu} = \frac{\int_{\Sigma_{nu}} (\tau_y - \tau_d)\frac{d_c}{2} d\Sigma_{nu}}{\int_{\Sigma_{nu}} s_i d\Sigma_{nu}}. \tag{8}$$

where $\Sigma_{nu}$ is the effective nucleation area, defined as the elements where the SSE-induced initial shear stress $\tau_0$ overcomes the assumed frictional strength $\tau_y$. $s_i$ denotes the area of the element $i$.

We calculate the total fracture energy ($E_G$) by integrating over elements on the fault for which the final slip distance $\delta_f \geq d_c$:

$$E_G = \int_{\Sigma} (\tau_y - \tau_d)\frac{d_c}{2} d\Sigma. \tag{9}$$

where $\tau_d$ and $\delta_f(x)$ refer to the final stress and slip on the rupture area ($\Sigma$), respectively, where the final slip is larger than $d_c$.

The average fracture energy $\bar{G}_c$ is defined as the average of the selected rupture area as

$$\bar{G_c} = \frac{E_G}{\int_{\Sigma} s_i d\Sigma}, \tag{10}$$

where $s_i$ is the area of the fault element $i$.

Stress drop can be defined as the difference between the dynamic rupture initial and residual shear stresses. We calculate the average stress drop across the rupture area using two methods:

1. as a spatially averaged stress drop $\overline{\triangle\tau_A}$ defined as

$$\overline{\triangle\tau_A} = \frac{\int_\Sigma \triangle\tau d\Sigma}{\int_\Sigma d\Sigma}, \tag{11}$$

where $\overline{\triangle\tau_A}$, $\triangle\tau$ and $\Sigma$ represent spatially-averaged stress drop, local stress drops, and rupture areas across the fault, respectively;

2. as an average stress drop based on energy considerations(Noda et al., 2013; Perry et al., 2020) as

$$\overline{\triangle\tau_E} = \frac{\int_\Sigma \triangle\tau\delta_f(x)d\Sigma}{\int_\Sigma \delta_f(x)d\Sigma}, \tag{12}$$

where $\overline{\triangle\tau_E}$ is the energy-based stress drop, and $\delta_f(x)$ is the final slip at each point $x$ of the fault.

### 2.4 Fault geometry and computational meshes

We build the model using the slab geometry inferred from the Middle America Seismic Experiment (MASE) (Pérez-Campos et al., 2008) (Figure 1b). MASE provided the high-resolution upper continental structure of the central Mexican subduction using routine methods, including receiver functions and seismic velocity tomography. The fault geometry is constructed from inferred depth contours with a depth spacing of 5 km and smoothed slightly to avoid potential numerical artifacts, such as those caused by abrupt changes in dip angles. We use the standard global projection WGS84/UTM, zone 11N to Cartesian coordinates.

We use the same fault geometry but different spatial extents and resolutions of the computational meshes in the SSE and dynamic rupture simulations to ensure adequate resolution. In the SSE model, we discretize the 450 km-long and 55 km deep slab interface into triangular elements of no more than 1,500 m edge length using the commercial software Trelis (`https://csimsoft.com/trelis`). The slow-slip cycle models require ∼10 h on 1536 cores for a 250-year-long SSE simulation on SuperMUC-NG at the Leibniz Supercomputing Centre in Garching, Germany.

For the dynamic rupture simulations, we focus on a sub-region of a length of 200 km along-strike. The rupture area of the $M_\mathrm{w}$ 7.3 Guerrero earthquake (Figure 1a) is smaller than the 450 km-long fault used for the SSE cycle model. We use the same slab geometry but additionally add topography during the generation of a volumetric tetrahedral mesh suitable for dynamic rupture earthquake simulations with SeisSol (Figure 1b) ). We incorporate topography data at 1-arc-minute spatial resolution from the *ETOPO1* model (https://www.ngdc.noaa.gov/mgg/global/) in a cubic domain of

500 km × 500 km × 200 km which is large enough to avoid any spurious reflected waves from the sides and bottom of the model domain.

It is crucial to ensure sufficiently high on-fault resolution to resolve the dynamic process zone (Day, 1982), the width of which varies in space and time, and with the initial conditions that affect the total available fracture energy and rupture velocity (Wollherr et al., 2018). For our preferred dynamic rupture scenario, we measure the average size of the dynamic process zone to be ∼1800 m. We choose slab interface element edge lengths of no more than 400 m, which is sufficient to resolve the process zone in our 4th-order accurate simulations (Day et al., 2005; Wollherr et al., 2018). The volumetric tetrahedral mesh is generated using SimModeler from *SimMetrix* (http://www.simmetrix.com/), which is free for academic use. The mesh is coarsened based on the distance normal to the fault surface at a graduation rate of 0.3, reducing the resolution for outgoing seismic waves for efficiency. The topographic surface is discretized using triangles of at most ∼2,000 m in length. Our resulting mesh for all shown dynamic rupture simulations consists of 11,764,144 elements in total. All simulations were performed on SuperMUC-NG at the Leibniz Supercomputing Centre in Garching, Germany. A simulation of 4th-order accuracy for 90 s duration requires 2800 CPU hours.

# 3 Results

## 3.1 The 2014 $M_w$ 7.6 slow-slip event on the curved and fluid-rich flat slab of the Guerrero Gap

We model episodic slow-slip cycles spontaneously emerging under long-term geological loading along the curved slab interface of the Guerrero Gap (Section 2.1). The long-term tectonic loading, which accumulates fault shear stresses, is balanced by the fault strength which is defined from a laboratory-derived rate-and-state friction law (Section 2.1.2). We constrain the fault frictional parameters by combining laboratory experiments on wet gabbro gouges (He et al., 2007) with a 2D steady-state thermal model constrained by P-wave seismic tomography (Manea & Manea, 2011). We extend a previous model that focused on the deeper part (10 km - 60 km depth) of the slab covering episodic SSEs only (Perez-Silva et al., 2021). Here, we consider the geometrically complex slab up to the trench and thus include the entire seismogenic zone (5 km - 60 km depth). We account for elevated pore fluid pressure atop the oceanic plate which locally reduces fault strength and eventually leads to episodic slow-slip emerging between depths of 20 km and 45 km (Section 2.1.1, Figure 2). This elevation of pore fluid pressure has been suggested based on the seismically inferred high $Vp/Vs$ ratios in central Mexico (Song et al., 2009) as well as in other subduction zones (Shelly et al., 2006; Audet et al., 2009).

We model cycles of long-term SSEs that occur repeatedly every four years. Figure 3 shows exemplary snapshots of the fault slip rate in the modeled scenario of the 2014 SSE. Each SSE episode lasts for up to 12 months (Radiguet et al., 2012) and reaches a peak slip rate of up to $10^{-6}$ m/s (Figure 3a,c,e). Our numerical results match the region-specific source characteristics of long-term SSEs inferred from geodetic inversion using the regional GPS network (Radiguet et al., 2016) (Supplementary Table S1). We attribute the good match of the first-order SSE characteristics to the realistic flat slab geometry and assumed near-lithostatic pore fluid pressure (Li & Liu, 2016; Perez-Silva et al., 2021). We select four sequential SSE episodes of our model, closely corresponding to the four geodetically recorded events in 2001/2002, 2006, 2009/2010, and 2014. We calculate the horizontal and vertical components of synthetic surface displacements at regional GPS stations and compare them with geodetic inversions (Radiguet et al., 2012; Gualandi et al., 2017b). The comparison between the synthetic and observed GPS vectors during the 2014 SSE is shown in Figures 3g-h and for the three earlier SSE episodes in Figure S4. All modeled SSE events yield good agreement with geodetic observations, although only dip-slip is considered in our simulations(Li & Liu, 2016).

The 2014 SSE initiates simultaneously at the eastern and western edges of the Guerrero Gap at a depth of 40 km. Both slip fronts migrate towards the center at a rate of 0.5 km/day (Figures 3a and 4b). The megathrust slips at a higher rate after the coalescence of the migrating fronts in the center, and the SSE then bilaterally propagates across the entire fault between 25 km and 40 km depth. However, we observe no immediate coseismic slip nucleating upon coalescence of the SSE fronts (between a depth of 20-45 km). This is different from the results of earlier 2D planar fault simulations (Kaneko et al., 2017) but in agreement with recent on- and off-shore observations that find no evidence of coseismic rupture due to collapsed slow-slip migrating fronts in the Guerrero Gap (Plata-Martinez et al., 2021).

Figure 4 shows the time-dependent evolution of the on-fault shear-to-effective-normal traction ratio and along-strike migration speed during the cycle of all four SSEs. During the quasi-periodic emergence of the SSEs, we find that fault shear tractions overall increase down-dip of the seismogenic zone (below a depth of 20 km). However, this increase is not steady and varies considerably with the acceleration of the migrating slip fronts. The space-time evolution of the traction ratio, defined as the shear over effective normal stress during the modeled transient slip, is shown in Figures 3b,d, and f. Here, the traction ratio increases gradually from down-dip (30 km depth) to up-dip (20 km depth) and eventually reaches 0.64 in the hypocentral area of the 2014 $M_{\mathrm{w}}$7.3 earthquake at a depth of 22 km, which is slightly shallower than that inferred by the USGS (Figures 3f and 4a).

The migrating 2014 SSE front moves slowly until day 267 and accelerates to 3.0 km/day at day 317 (Figure 4b). This acceleration, associated with rapid strain energy release, eventually increases shear stress at the down-dip end of the seismogenic zone in our model (see Figure 4c and Movie S2). The migration speed can vary depending on the temporal stress evolution during the modeled SSE, which results in various values of traction ratio below the locked zone between different slow-slip cycles (Figure S3). Accelerating SSE fronts, as in our 2014 SSE model, have been observed before the 2014 Chile earthquake (Socquet et al., 2017a) and before larger earthquakes in Japan (Uchida et al., 2016), which was suggested as a potential precursory signal indicating megathrust earthquake nucleation.

In contrast, traction ratios increase considerably less during the earlier three modeled SSEs (blue lines in Figure 4a and blue-to-purple lines in Figure S2). Shear stresses temporally increase during the 2001/2002 and 2006 SSEs but decrease during the 2009/2010 event. For example, the peak traction ratio in the 2014 episode is about 3.23% higher than in the preceding 2009-2010 event, cor-

responding to a 0.1 MPa increase in shear stress. We highlight that the long-term increase of the peak traction ratio at the hypocentral depth during the 20-year-long simulation is small compared to the transient traction changes during the 2014 SSE (Figure 4a). None of the three earlier events leads to traction ratios large enough to overcome the (prescribed) frictional fault strength in the seismogenic part of the slab in our preferred dynamic rupture model.

### 3.2 Earthquake initiation and dynamics accounting for slow-slip transient stresses

We present the first 3D dynamic rupture model of the 2014 $M_{\mathrm{w}}$ 7.3 Guerrero earthquake. Our rupture scenarios are informed by the transient stress of preceding slow slip events and additional predefined frictional heterogeneity on the fault. We focus on a preferred model (Section 2.2; Figure 5) that reproduces the key features of geophysical observations and provides physically self-consistent descriptions of earthquake initiation, dominantly governed by SSE-induced shear stress changes, and its dynamics and arrest, which are predominantly governed by predefined frictional asperities. We discuss alternative rupture scenarios probing sensitivity to initial conditions in Section 4.2.

We constrain the initial shear stress, normal stress, and pore fluid pressure before the earthquake using our long-term slow-slip cycle model on the same slab geometry (Section 2.2.1). We extract the SSE model state when the traction ratio, which is associated with the SSE fronts, peaks (Figure 4) to inform the dynamic rupture simulation. We use a linear slip-weakening friction law (Andrews, 1985) to describe the co-seismic fault strength and yielding (Section 2.2.3). Choosing a small critical slip-weakening distance of $d_c$=0.05 m, which is at the lower limit of seismological observations (Mikumo et al., 2003) and the upper limit of laboratory-inferred estimates (Marone, 1998), allows for spontaneous SSE-initiation at the same time as a sustained large earthquake rupture. We assume a statically strong fault (static friction coefficient $\mu_s = 0.626$) in agreement with the high static frictional strength of rocks (Byerlee, 1978) but effectively weakened by high pore fluid pressure. This specific choice of $\mu_s$ allows us to model realistic co-seismic rupture dynamics and arrest, including realistic levels of slip, rupture speed, and stress drop, as well as spontaneous nucleation at 22 km due to the modeled 2014 SSE event. An alternative, less realistic model with smaller $\mu_s$ is shown in Fig S11 and will be discussed in Section 4.2.

Although earthquake nucleation is linked to the transient stress of the SSE cycle, we show that capturing realistic rupture propagation and arrest requires additional heterogeneity of the megathrust slab. We show that including two circular frictional asperities (Section 2.2.3 can reproduce the observed co-seismic characteristics to first-order. We vary the maximum possible frictional strength

drop smoothly within each asperity: the dynamic friction coefficient $\mu_d$ gradually increases at the edge of the asperities. High variability of dynamic friction has been reported in relation to fault materials and sliding rates in laboratory experiments (Di Toro et al., 2004; Collettini et al., 2019) and has been shown to largely affect coseismic rupture dynamics on crustal faults in numerical models(Ramos & Huang, 2019; Aochi & Twardzik, 2020; Tinti et al., 2021).

In our earthquake model, self-sustained dynamic rupture nucleates spontaneously at a depth of 22 km, where the modeled 2014 SSE front acceleration leads to a local increase in shear traction (Figure 4a,c). This location agrees with the observationally inferred hypocenters within their uncertainties (Figure 5a-b). Unlike typical dynamic rupture models, where nucleation is prescribed ad hoc (Galis et al., 2014, e.g.,), spontaneous runaway rupture is here initiated merely by the locally increased shear stress of the preceding SSE transient. Our rupture model dynamically breaks the central asperity and subsequently migrates to the second patch under slightly increasing slip rates (Figure 5 and Movie S3). The rupture arrests smoothly at the boundaries of the prescribed frictional asperities. The final rupture area is located up-dip from the hypocenter and has no clear overlap with the area that hosts aseismic rupture during slow-slip (Fig S6).

Our preferred earthquake simulation resembles the key observed seismic and geodetic characteristics within observational uncertainties (Figures 6a-e). Two broad peaks in the moment release rate emerge in our dynamic rupture model, as inferred from teleseismic inversion using more than 70 stations across $35^o-80^o$ epicentral distance(Ye et al., 2016) (Figure 6a). This suggests a multi-asperity rupture process, including dynamic triggering and delays between different asperities (Figure 6f). In our rupture dynamics model, the first and second peaks appear closer in time than inferred in the inversions which may reflect additional complexities on natural faults and observational uncertainties. For example, the shape of the second asperity area may be varied in our dynamic rupture model to better match the observed moment rate release timing. However, teleseismic inversion lacks the adequate resolution to better inform on the spatial extent of slip (Ye et al., 2016). Our modeled total cumulative moment release is $9.41 \times 10^{19} Nm$, which corresponds to a moment magnitude of $M_{\mathrm{w}}$ 7.28 and agrees well with the observations (Figure6a). An alternative dynamic rupture model with only a single asperity (Section 4.2; Figure 7) fails to reproduce a realistic moment magnitude and the pronounced two-peak character of the moment rate release. Because both dynamic rupture models spontaneously initiate due to the same transient SSE stresses but strongly differ in co-seismic dynamics, we conclude that additional frictional heterogeneity is required to model the propagation dynamics and arrest of the Guerrero earthquake.

Geodetic inversion using permanent on-shore GPS stations yields smaller slip amplitudes (Gualandi et al., 2017b) but a larger rupture area extending up to the trench, compared to teleseismic inversion (Ye et al., 2016) (Figures 6c-d). Similarly, our modeled dynamic rupture features shallow fault slip up-dip of the hypocenter, while our maximum slip amplitude is 2.5 m (Figure 6e), which is consistent with teleseismic inversion assuming $V_r = 2.5$ km/s (Ye et al., 2016). We note that the differences in geodetic and teleseismic fault slip inversions are likely affected by limitations in data resolution and differences in the assumed source time functions, velocity models, and/or fault geometries. Figure 6b shows the modeled static surface deformation at 80 s after the rupture initiation and its comparison with geodetic observations (Gualandi et al., 2017a). There are only two GPS stations (ZIHP and PAPA) with clear recorded signals close to the rupture area and one station (TCPN) with a smaller-amplitude signal distant from the epicenter. Our synthetic surface displacements at ZIHP and PAPA are consistent with the reverse plate movement direction but slightly higher in amplitude than those observed.

Our preferred two-asperity dynamic rupture model reproduces both seismic and geodetic characteristics and is consistent with the localized slip heterogeneity inferred from seismic imaging using regional networks (Song et al., 2009; Plata-Martinez et al., 2021). Given the sparsity of co-seismic seismic and geodetic observations, we judge our forward model as data-justified first-order illumination of rupture dynamics and arrest. We note that future incorporation of a high-resolution regional velocity model may improve the achieved observational match.

We analyze the stress drop and energy budget of our preferred dynamic rupture model accounting for the preceding slow-slip cycle with respect to event-specific and global observations (Section 2.3). We calculate the average co-seismic stress drop in two different ways: 1) by spatially averaging the on-fault stress drop, and 2) by averaging the modeled stress drop based on energy considerations (Noda et al., 2013; Perry et al., 2020) . The two approaches result in average model stress drops of 1.74 MPa and 2.1 MPa, respectively. These values are within the expected uncertainties (Abercrombie, 2021) of the seismological inference of 2.94 MPa (Ye et al., 2016) and are consistent with the global average of the inferred megathrust earthquake stress drops (Abercrombie & Rice, 2005).

Next, we analyze the earthquake initiation energy budgets accounting for the transient stress shadowed by the preceding SSE. We calculate the average fracture energy across the effective nucleation area directly induced by our modeled 2014 SSE in the hypocentral area as 0.17 MJ/m$^2$ (Section 2.3). This inference is comparable to the range of nucleation energies (0.1-1 MJ/m$^2$) estimated for most

$M > 8$ Nankai earthquakes in southwestern Japan (N. Kato, 2012), implying that the transient stresses of aseismic slip may play a ubiquitous role in the nucleation of megathrust earthquakes. In comparison, the dynamic rupture fracture energy averaged across the entire co-seismically slipping fault is only 0.11 MJ/m$^2$. This is about 35% lower than the SSE fracture energy at the hypocenter governing the nucleation stage and similar to a seismologically inferred global average of 0.1-10 MJ/m$^2$ (Abercrombie & Rice, 2005), but 45% lower than the range of 0.2-2.0 MJ/m$^2$ measured on natural crustal faults (Tinti et al., 2005). This relatively low overall fracture energy is consistent with the low average stress drop, which results from the assumed elevated pore fluid pressure constrained by regional seismic imaging (Song et al., 2009). The elevated pore fluid pressure at depth is crucial for recovering faulting dynamics during both the long-term SSE and short-term initiation of our dynamic rupture model.

## 4 Discussion

### 4.1 Transient influence of slow slip on the initiation of megathrust earthquake

Our dynamic rupture models of the $M_w$7.3 Guerrero earthquake initiated by quasi-dynamic models of the preceding long-term SSE cycles illustrate the interaction between aseismic and co-seismic fault slip. It has been suggested that slow slip at the down-dip end of the seismogenic zone transfers shear stresses up-dip (Liu & Rice, 2007) or temporally aid up-dip pore fluid migration (W. Frank et al., 2015), both of which potentially destabilize the locked portion of the megathrust. We find that the transient increase in the shear-to-effective-normal-stress ratio resulting from the accelerating migration of the preceding slow-slip events can lead to the spontaneous initiation of realistic earthquake rupture and that this process is sensitive to the dynamics of the long-term transient SSE cycle.

In our model, the increasing transient shear stress is sufficiently high for spontaneous dynamic rupture without additional weakening mechanisms, such as the effects of thermal pressurization (Noda et al., 2009). However, accounting for additional co-seismic weakening may further aid the slow-slip transient initiation of dynamic rupture (Hirono et al., 2016) inherently capturing our here prescribed variability of co-seismic frictional strength drop (Perry et al., 2020). Similarly, a recent conceptual model combining shallow SSEs and two asperities finds that the time-dependent balance between stress and strength is complex and not all SSEs directly lead to the nucleation of an earthquake (Meng & Duan, 2022), even when no geometrical complexity or pore fluid variation is considered.

### 4.2 Alternative dynamic models with varying asperities

Accounting for megathrust asperities in our co-seismic dynamic rupture model is important for reproducing observationally inferred first-order source characteristics. Our preferred dynamic rupture scenario includes two frictional asperities (Figure 6f), which vary in their local dynamic friction coefficient from the surrounding slab interface, as proxies of megathrust heterogeneity governing the co-seismic rupture complexity. In the following, we show two selected alternative dynamic rupture scenarios that illustrate the sensitivity of our SSE-initiated co-seismic rupture dynamics to prescribed frictional asperities.

#### *4.2.1 Model A2: two rupture asperities with higher initial shear stress*

In dynamic rupture simulations, asperities due to locally reduced dynamic frictional strength lead to similar rupture behavior as asperities of elevated initial shear stress due to the equivalent fracture energy (Tinti et al., 2021). Here, we present an alternative dynamic rupture model, Model A2, with a constant dynamic friction coefficient but heterogeneous initial shear stress. The initial shear stress is smoothly reduced outside both rupture asperities, which leads to spontaneous rupture arrest. We use the same spatial exponential function $G_1(r_1, r_2)$ defined in Section 2.2.3 to decrease shear stresses smoothly outside the two geometrically equivalent pre-assigned rupture asperities. We set the initial shear stress as $\tau_0^{A2} = \tau_{sse} \times G_1(r_1, r_2)$ where $\tau_{sse}$ refers to the on-fault shear stress linked from the SSE cycle model (Figure S8a). This setup leads to a localized distribution of the shear-to-effective-normal-stress ratio near the USGS catalog hypocenter (Figure S8b).

The modeled source characteristics of the earthquake, including moment release, magnitude, slip distribution, and surface deformation, are all similar to our preferred model (Figure S10), except for a slightly sharper peak in moment release, corresponding to rupture arrest, than that of our preferred model (Model A1). We conclude that, in principle, local shear-stress asperities can lead to equivalent SSE-initiated rupture dynamics compared to frictionally-weak asperities.

#### *4.2.2 Model B1: a single rupture asperity with reduced dynamic friction coefficient $\mu_d$*

Next, we demonstrate the sensitivity of rupture dynamics and synthetic observables (e.g., moment rate release) to megathrust heterogeneity using a single circular asperity wherein the dynamic frictional strength locally decreases (Model B1).

We examine a model with a single asperity with varying $\mu_d$ on the fault. We manually introduce an exponential taper function, call $G2(r_1)$ similar to $G_1$ defined in Secion 2.2.3 on the fault. The distribution of dynamic friction shaped according to function $G2$ is shown in Figure 7a.

$$G_2(r_1) = \begin{cases} 4/3.0 * min(0.75, \exp(\frac{r^2}{r^2 - r_{c1}^2}) \; r1 \leq r_{c1} \\ 0 \; otherwise \end{cases}$$

where $r_{c1}$ are 38 km , $r_i = \sqrt{(x - x_i)^2 + (y - y_i)^2}, i = 1$. The positions of centers are listed in Table S2. The results of Model B2 are shown in Figures 7b-d.

The resulting moment magnitude is only $M_{\mathrm{w}}7.15$, and the moment rate release features a single sharp peak instead of reproducing the observed characteristic two-peak shape (Figure 7c). The modeled spatial extents of the fault slip and surface displacement amplitudes are significantly smaller (Figures 7b,d).

### 4.3 Variation in fault asperities and its implication for seismic hazard

Megathrust asperities have been related to depth-varying seismic and aseismic faulting behaviors (Lay et al., 2012; Walton et al., 2021). While we here parameterize both asperities as dynamically weak (low $\mu_d$), heterogeneity in the initial stresses, structure, effective static fault strength, or pore fluid pressure (Bilek & Lay, 1999; Bürgmann, 2018) may serve as dynamically viable asperities (Ramos & Huang, 2019; Harris et al., 2021; Tinti et al., 2021; Madden et al., 2022) and additional observations are required to distinguish between them. We show that local shear-stress asperities can lead to equivalent rupture dynamics in Section 4.2 and Figure S10. Our parameterization of frictional asperities is relatively simple but effective in reproducing first-order characteristics within the uncertainties of sparsely observed earthquake kinematics. Denser regional seismic and geodetic instrumentation along the central Mexican coast and off-shore, allowing for better imaging of coseismic fault slip, would be crucial to inform and validate data-integrated and physics-based modeling.

Our choice of frictional parameters in the dynamic rupture model allows for balancing the depth-dependent fault strength, heterogeneous initial shear stresses, and heterogeneous frictional strength drop to achieve realistic levels of coseismic slip and moment release across a relatively small rupture area in dynamic rupture simulations. This sensitivity is exemplified in Figure S11a where a slightly lower $\mu_s$ results in delayed rupture arrest, a larger rupture area, and over-prediction of the ampli-

tude and arrival of the first peak in the modeled moment release. Although simpler than the rate-and-state friction law used in the long-term SSE cycle simulations, we yield a similar range in reference friction coefficients (Figure S11b) and comparable behavior in coseismic slip.

Our modeled SSE and coseismic fault slip are located largely off-shore in central Mexico, where a dense array of ocean bottom seismometers (OBS) has discovered episodic shallow tremors, suggesting small-scale slow-slip events or low-frequency earthquakes (Plata-Martinez et al., 2021) potentially linked to small asperities up-dip of the slow-slip region. Accounting for additional small-scale heterogeneity on the fault may help explain high-resolution observations, such as complexity in moment release rate and strong ground motions (Galvez et al., 2016) Here, we focus on the one-way interaction between the SSE cycle and dynamic rupture and omit the respective influence of coseismic rupture on slow-slip transients. Modeling 3D fully dynamic earthquake cycles on geometrically complex faults (Jiang et al., 2022; Erickson et al., 2023; Uphoff et al., 2023) that incorporate spontaneous (aseismic) nucleation, dynamic rupture, and post-seismic deformation are computationally challenging but are becoming achievable at realistic scales and levels of complexity to allow for direct observational verification. Extending our approach to a unified and fully coupled slow-slip and dynamic rupture framework is a promising future step.

## 5 Conclusions

Our mechanically self-consistent and data-driven 3D models of long-term SSE cycles, megathrust earthquake initiation, and rupture dynamics in the Guerrero Seismic Gap contribute to a better understanding of the earthquake generation process and can potentially lead to improved time-dependent operational earthquake forecasting (Uchida & Bürgmann, 2021). By incorporating the transient stress evolution of slow-slip before coseismic rupture and asperities in co-seismic friction drop, our models reproduce the kinematic and dynamic characteristics of both aseismic slip and coseismic rupture and reveal their physical link. Although long-term stress does not continuously accumulate, the accelerating migrating SSE fronts transiently increase shear stress at the down-dip end of the seismogenic portion of the megathrust. Improvements in the detection of transient aseismic slip deformation will aid in assessing seismic hazards in coastal regions (A. Kato et al., 2012; Socquet et al., 2017b). Furthermore, identifying distinct acceleration signals might be routinely possible in future regionally dense networks, specifically off-shore (Hilley et al., 2022).

## 6 Acknowledgements

This work was supported by the European Research Council (ERC) under the European Union's Horizon 2020 research and innovation programme (TEAR, Grant agreement No. 852992). The authors acknowledge additional support by the National Science Foundation (Grant No. EAR-2121666), the National Aeronautics and Space Administration (80NSSC20K0495), and Horizon Europe (ChEESE-2P grant agreement No. 101093038, DT-Geo grant agreement No. 101058129, and Geo-Inquire grant agreement No. 101058518). Computing resources were provided by the Leibniz Supercomputing Centre (LRZ, project No. pr63qo and No. pr49ha on SuperMUC-NG) and by the Institute of Geophysics of LMU Munich (Oeser et al., 2006). We thank Andrea Perez-Silva for a number of initial tests during her Master thesis. We thank Dr. Mathilde Radiguet for kindly sharing the GPS inversion results of the Guerrero slow slip event. We appreciate the fruitful discussion with Dr. Yoshihiro Kaneko, Dr. Luis Dalguer, and the seismology group at Munich University (LMU).

## 7 Open Access

We use TriBIE (`https://github.com/daisy20170101/TriBIE`) for the slow slip simulation and SeisSol Master branch, available on GitHub (`github.com/SeisSol/SeisSol`) for dynamic rupture simulation. How to download and run the code is described in the SeisSol documentation (`seissol.readthedocs.io/en/latest/`). We use the software SKUA-GOCAD (`pdgm.com/products/skua-gocad/`) as modeling environment to produce all 3D fault models. Earthquake source data of the 2014 Guerrro event is from USGS (`https://earthquake.usgs.gov/earthquakes/eventpage/usb000pq41/executive`) and GCMT (`https://www.globalcmt.org`). All input files and meshes required to reproduce the TriBIE long-term slow slip cycle and SeisSol earthquake dynamic rupture scenarios can be downloaded from`https://doi.org/10.5281/zenodo.6956697`.

**Table 1.** Physical parameters used in the quasi-dynamic slow-slip cycle simulations.

| Parameter | Symbol | Value | Unit |
|---|---|---|---|
| rate-and-state direct effect parameter[a] | $a$ | 0.01 - 0.02 | - |
| rate-and-state evolution effect parameter | $b$ | 0.0135 | - |
| characteristic slip distance (for SSEs) | $D_{RS}^{SSE}$ | 10.086 | mm |
| characteristic slip distance (for earthquakes)[b] | $D_{RS}^{dy}$ | 252.15 | mm |
| reference slip rate | $v_0$ | $10^{-6}$ | m/s |
| reference friction coefficient | $f_0$ | 0.6 | - |
| initial slip rate | $V_{ini}$ | $10^{-9}$ | m/s |
| initial state variable | $\theta_{ini}$ | 0.1 | s |
| critical nucleation size | $h_{RA}^{*}$ | 112.3 | km |
| quasi-static process zone size | $\Lambda_0$ | 11.8 | km |
| effective normal stress | $\bar{\sigma}_n$ | 50 | MPa |
| SSE effective normal stress | $\bar{\sigma}_n^{SSE}$ | 2.5 | MPa |
| lithostatic pressure | $\sigma_z$ | depth-dependent | MPa |
| pore fluid pressure | $p_f$ | depth-dependent | MPa |
| rock density | $\rho$ | 2670 | $g/m^3$ |
| shear modulus | $\mu$ | 30 | GPa |
| Poisson's ratio | $\nu$ | 0.25 | - |

[a] Parameter $a$ varies between velocity-weakening to velocity-strengthening

[b] Our SSE cycle simulations do not include earthquakes

**Table 2.** Linear slip-weakening friction parameters used in the dynamic earthquake rupture simulations.

| Parameter | Symbol | distribution | Value |
|---|---|---|---|
| static friction coefficient | $\mu_s$ | uniform | 0.626 |
| dynamic friction coefficient | $\mu_d$ | two asperities | 0.546 |
| critical slip distance | $d_c$ | uniform | 0.05 m |
| frictional cohesion | $c_0$ | depth-dependent | 1.0 - 0 MPa |

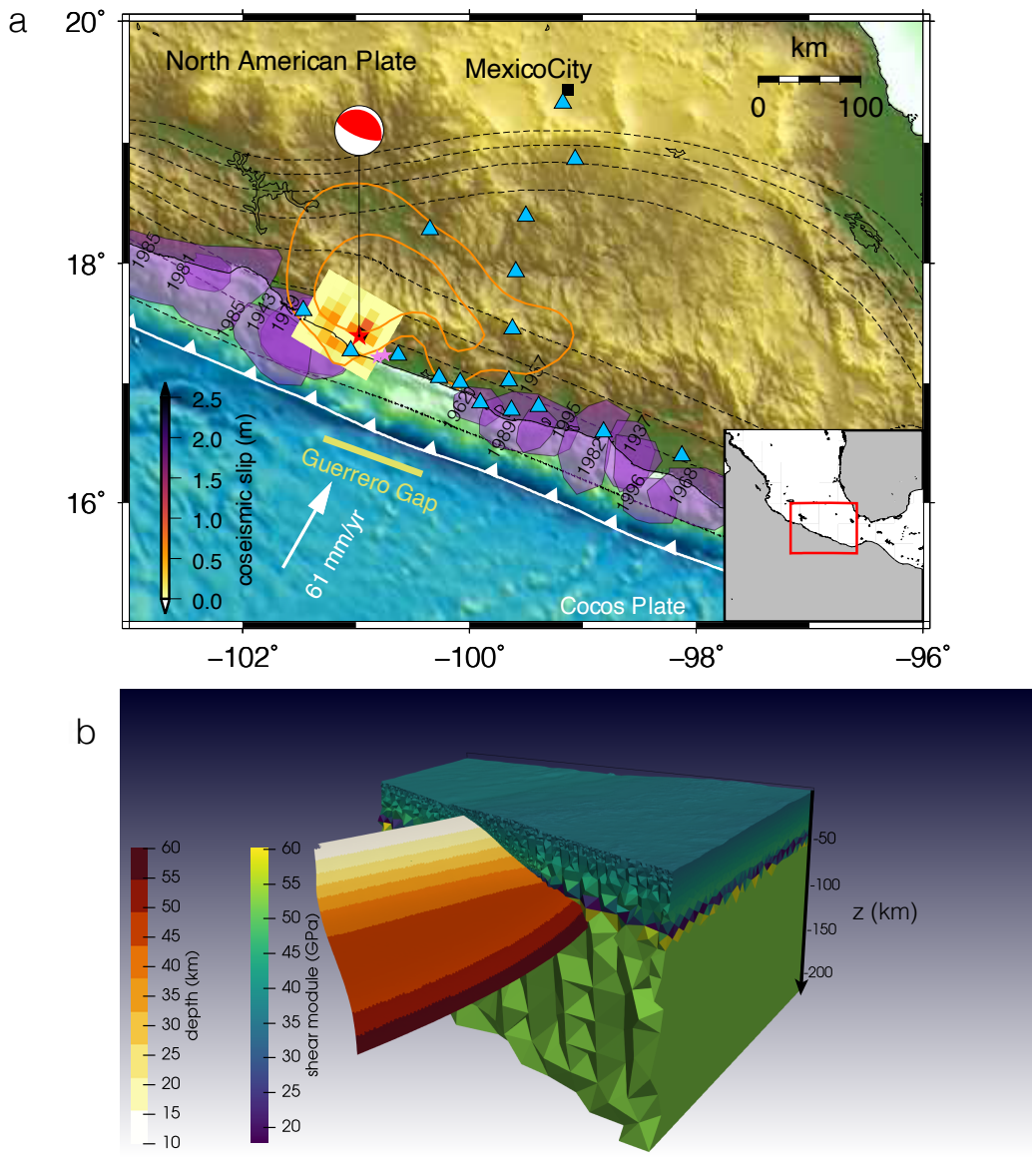


**Figure 1.** (a) Map of central Mexico where the Cocos plate subducts beneath the North American plate at a rate of 61 mm/yr (PVEL model(DeMets et al., 2010)). The so-called Guerrero Seismic Gap is a 100-km long segment between 100.2°W and 101.2°W (yellow bar) that lacks recent large earthquakes(Lowry et al., 2001). Purple shades indicate large ($M_w \leq 6.8$) earthquakes after 1940 (Lowry et al., 2001). The focal mechanism of the 2014 $M_w$ 7.3 Guerrero earthquake is shown in red (strike:304°, dip:21°, rake:99°, Global Centroid Moment Tensor catalog (GCMT)(Dziewonski et al., 1981; Ekström et al., 2012)). A finite coseismic source model using teleseismic inversion is shown as yellow-to-red-to-black rectangles (Ye et al., 2016). The orange contours indicate the 10 cm and 20 cm aseismic levels of fault slip during the 2014 $M_w$ 7.3 slow-slip events (Radiguet et al., 2016). The blue triangles mark the permanent GPS stations used in a geodetic inversion of both the coseismic and slow slip (Gualandi et al., 2017b). Depth contours from 5 km depth (trench) to 80 km depth are shown as dashed lines with 5 km depth spacing. Mexico City is shown in black. (b) Slab surface geometry extending from the trench to a depth of 60 km in both slow-slip cycle and dynamic rupture simulations. Tetrahedral elements are color-coded by a 1D layered velocity model from seismic imaging (Dougherty & Clayton, 2014) that is used in the dynamic rupture model.

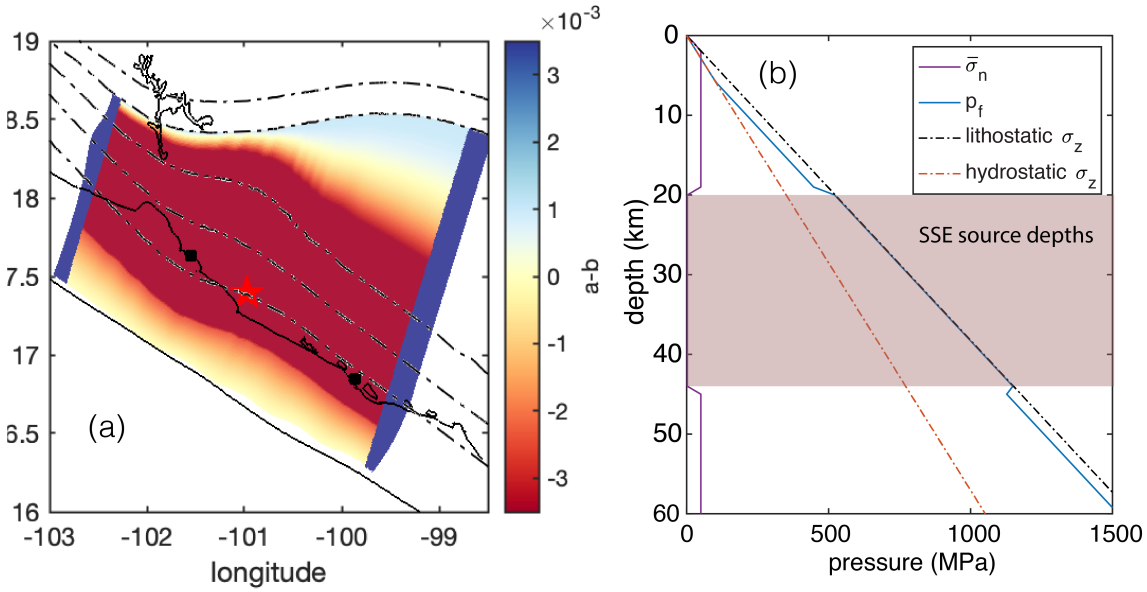


**Figure 2.** (a) Map view of the dimensionless frictional parameter $a - b$ on the fault. The distribution of $(a - b)$ at different temperatures was obtained from laboratory experiments on wet gabbro gouges (He et al., 2007). We project this temperature-dependent $(a - b)$ distribution onto the slab interface using the thermal profile from a 2D steady-state thermal model constrained by P-wave seismic tomography in central Mexico. The transition where $a - b = 0$ occurs at a depth of 42 km. (b) Along-depth profile of effective normal stress $\bar{\sigma_n}$ and pore fluid pressure $p_f$ used in both the SSE cycle and dynamic rupture models, and hydrostatic and lithostatic pressures $\sigma_z$ as references.

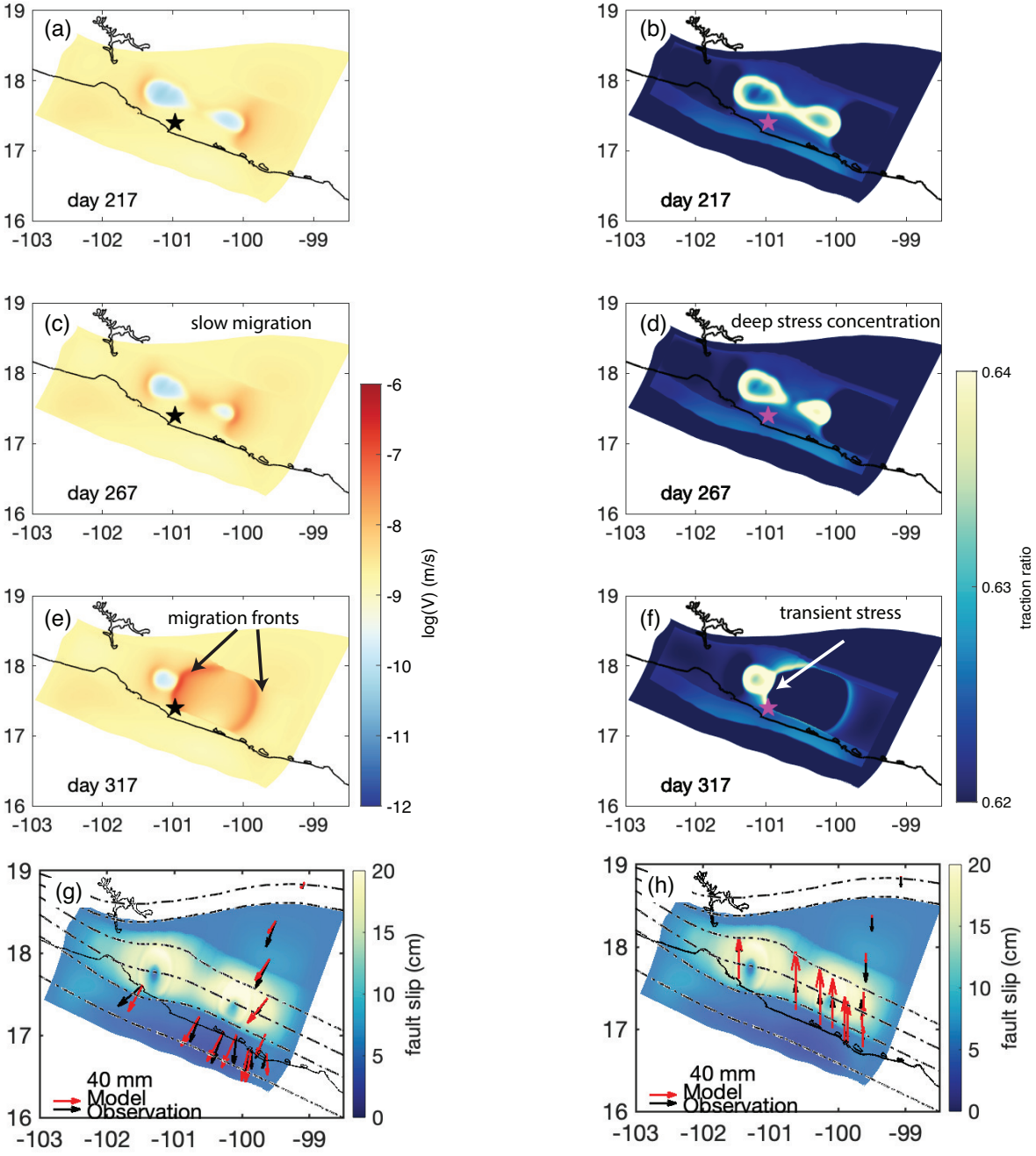


**Figure 3.** The 2014 SSE in the Guerrero Gap from the preferred quasi-dynamic slow-slip cycle model. Snapshots of fault slip rate (a,c,e) and traction ratios (b,d,f), defined as shear over effective normal stress, on days 217, 267, and 317, respectively. The black star marks the epicenter of the 2014 $M_w$ 7.3 Guerrero earthquake from National Earthquake Information Catalog (USGS NIEC) (https://earthquake.usgs.gov/earthquakes/eventpage/usb000pq41/executive ). Slow-slip fault slip rates can reach up to $10^{-6}$ m/s, which is 1000 times faster than the plate convergence rate ($V_{pl}$ =61 mm/yr). The time-dependent evolution of the fault slip rate is shown in Movie S1 (Supplementary Information). (g), (h): Modeled accumulated 2014 SSE fault slip distribution and surface GPS displacement.The black and red arrows show the observed (Gualandi et al., 2017a) and synthetic surface GPS displacements, respectively. Dashed black lines are the depth contours of the subducting slab from 20 km to 80 km depth with 20 km depth spacing.

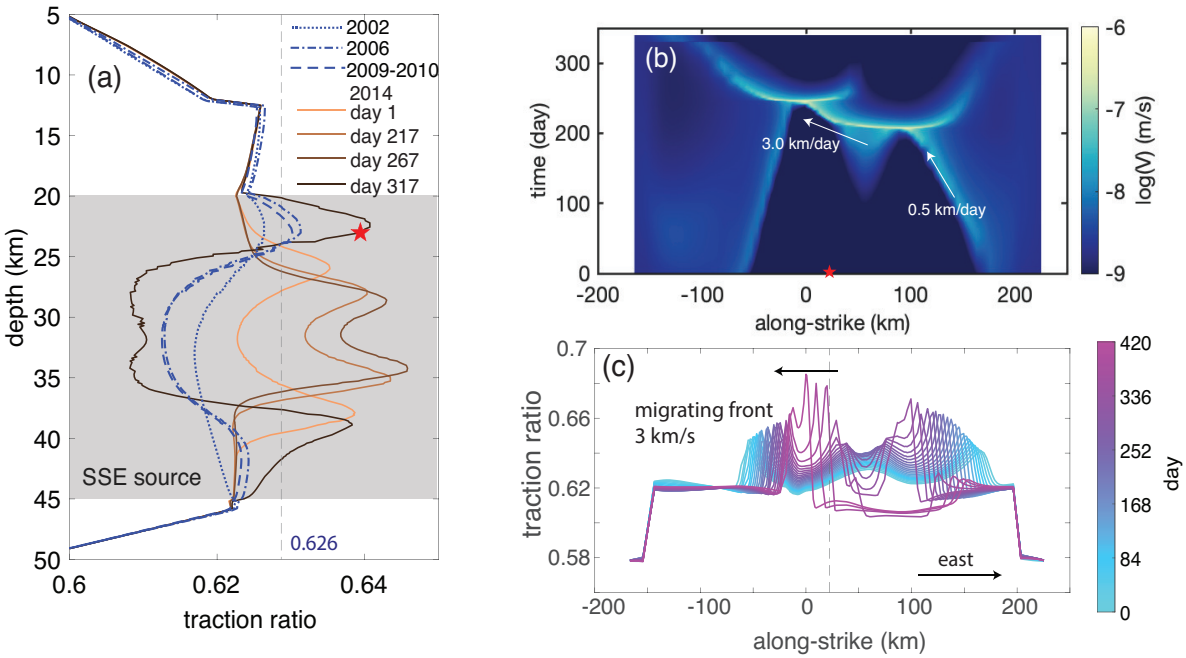


**Figure 4.** Time-dependent evolution of the on-fault shear-to-effective-normal traction ratio and along-strike migration speed during the modeled SSE cycle. The red star marks the USGS catalog hypocenter of the 2014 $M_w$7.3 Guerrero earthquake. (a) Cross-sections of the traction ratio during the four modeled subsequent SSEs. Colored solid lines indicate the traction ratios on days 1, 217, 267, and 317 of the modeled 2014 SSE. The blue dot-dashed and dot-dashed lines represent the traction ratios of the three SSE episodes in 2002, 2006, and 2009-2010, respectively. The dashed gray line indicates the static friction coefficient on-fault ($\mu_s = 0.626$) assumed in the dynamic rupture earthquake simulation. (b) Spatial and temporal evolution of the on-fault slow-slip rate along the 20 km depth contour. The white vectors indicate the averaged migrating speeds of the slip front at y=150 km and y=0 km. (c) Profiles of the traction ratio sampled every 10 days along the 30 km depth contour during the modeled SSE cycle illustrate the westward acceleration of the SSE migration front.

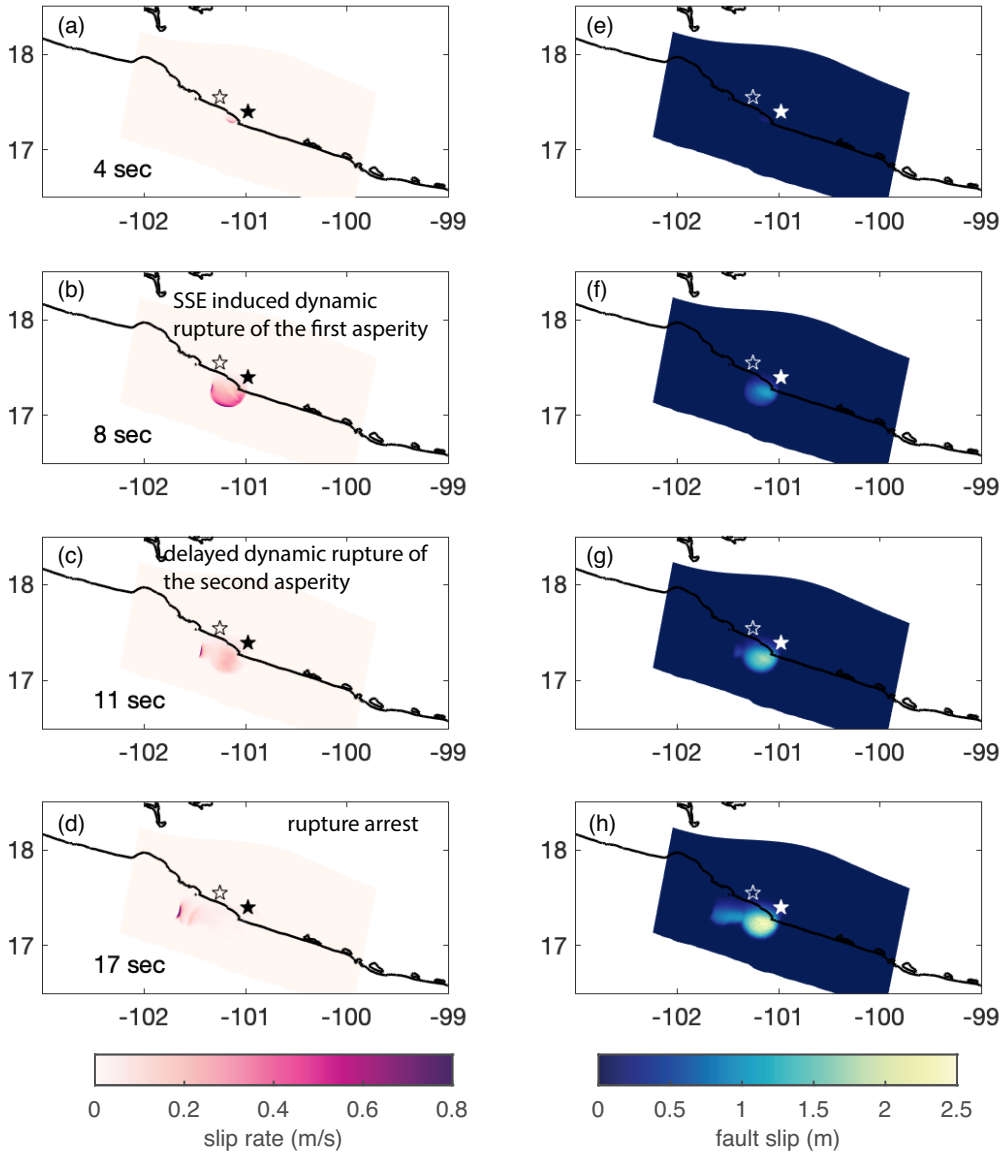


**Figure 5.** Preferred dynamic rupture model of the 2014 $M_w$ 7.3 Guerrero earthquake. Snapshots of the modeled coseismic fault slip rate (left panels) and fault slip (right panels) at 4 s, 8 s, 11 s, and 17 s, respectively. (a): spontaneous nucleation governed by shear stress transients of the long-term SSE cycle, (b): SSE initiated dynamic rupture of the first asperity, (c): delayed rupture of the second asperity, and (d): the dynamic arrest of rupture (Supplementary Movie S3). The corresponding fault slip at each time step is shown in (e)-(h), respectively. The coastline is indicated by the black line. Solid and empty stars indicate the different hypocenter locations from the USGS and GCMT catalogs, respectively.

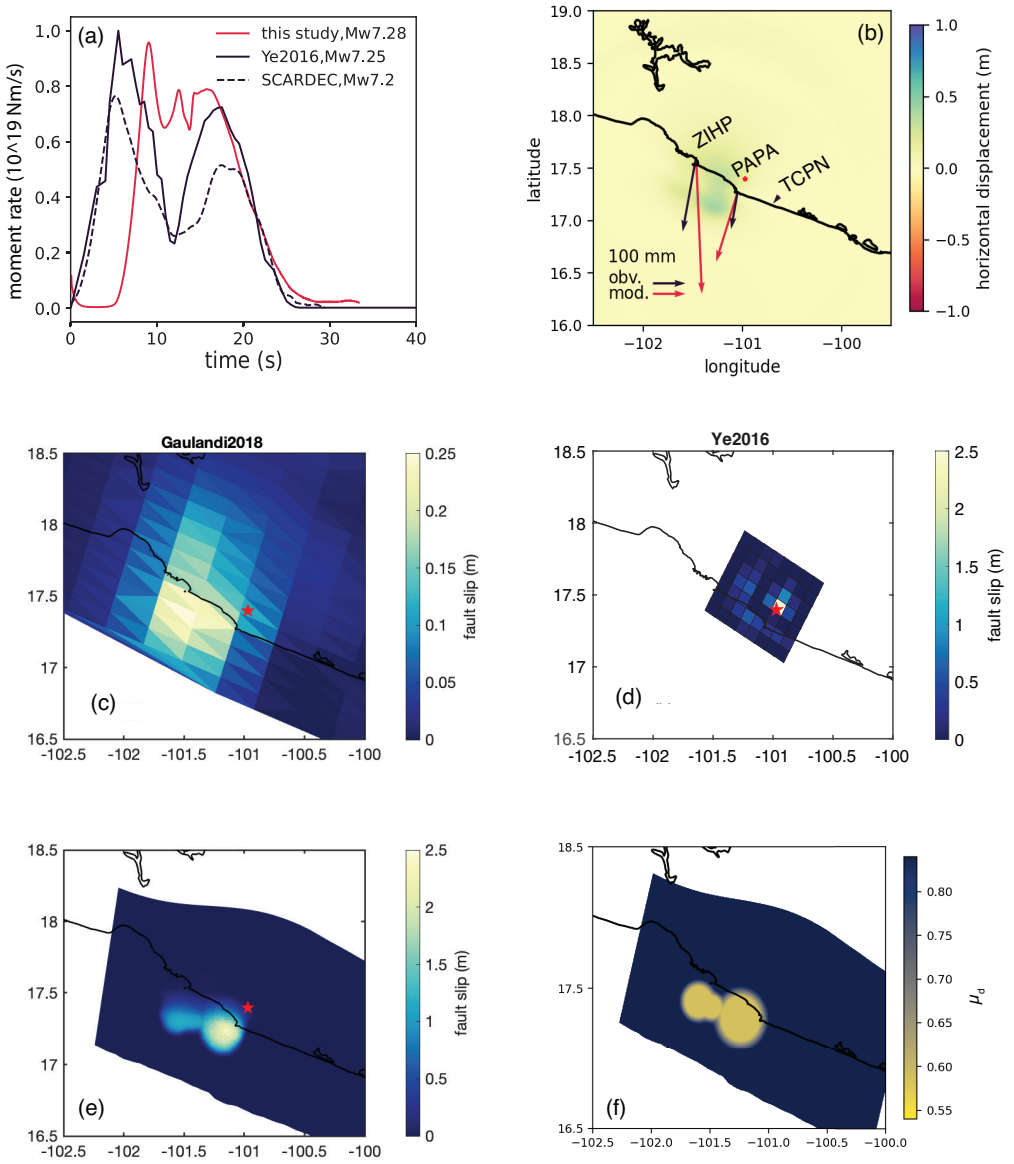


**Figure 6.** Observational verification of kinematic and dynamic source characteristics of the dynamic rupture model of the 2014 $M_w$7.3 Guerrero earthquake. (a) On-fault dynamic rupture moment rate compared to teleseismic inversion(Ye et al., 2016) and SCARDEC (http://scardec.projects.sismo.ipgp.fr) (Vallee et al., 2011). (b) Mapview with horizontal surface displacements observed at continuous GPS stations (black(Gualandi et al., 2017a)) and in our simulation (red). The red star marks the USGS catalog hypocenter. Accumulated fault slip from (c) regional geodetic inversion(Gualandi et al., 2017a), (d) teleseismic inversion(Ye et al., 2016), and (e) preferred dynamic rupture scenario. The maximum slip is 0.25 m, 2.5 m and 2.5 m, respectively. (f) Distribution of the prescribed heterogeneous dynamic friction coefficient $\mu_d$ which gradually increases from 0.546 within to 0.826 at the edge of the asperities following an exponential function (see Methods: "Linear slip-weakening friction").

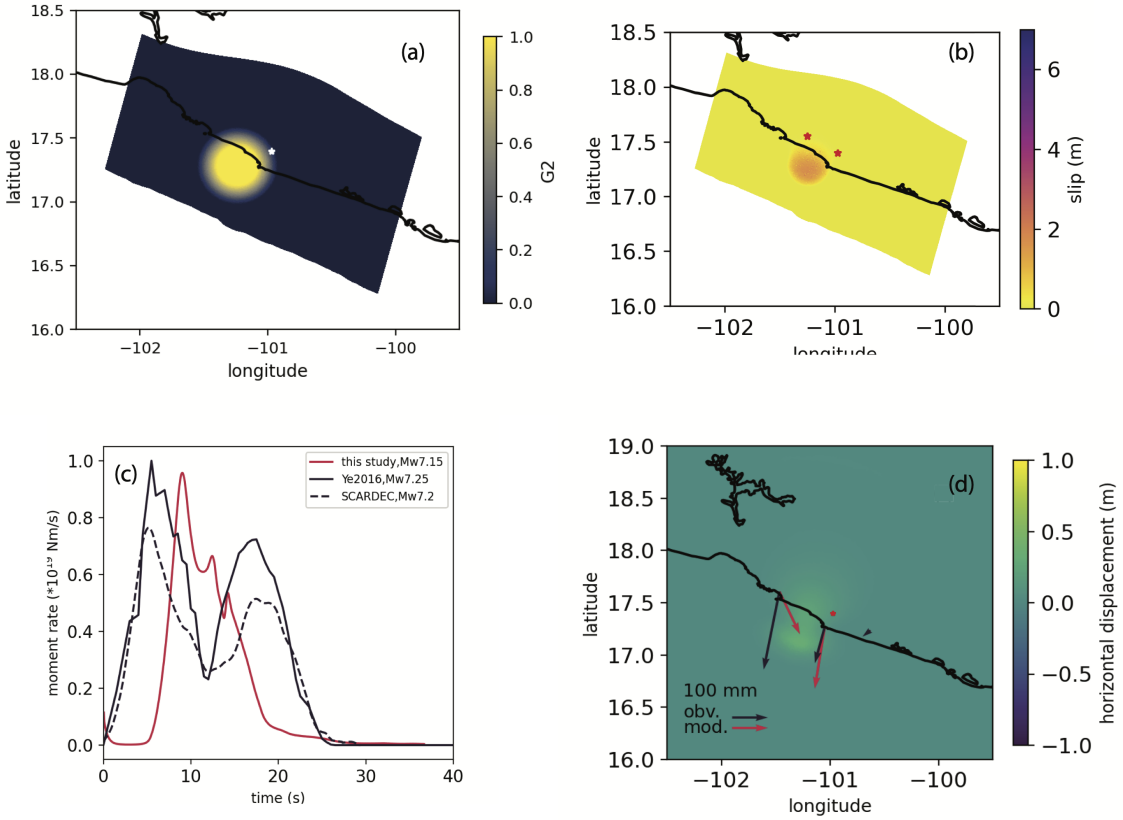


**Figure 7.** (a) Map view of the exponential function $G_2$ (defined in Supplementary Text S2) which we use to prescribe the single asperity of Model B1. (b) cumulative fault slip, (c) moment release rate, and (d) synthetic surface deformation of dynamic rupture Model B1 with a single asperity. The shown GPS stations are the same as in Figure 6b.

## References

Abercrombie, R. E. (2021). Resolution and uncertainties in estimates of earthquake stress drop and energy release. *Philosophical Transactions of the Royal Society A: Mathematical, Physical and Engineering Sciences*, *379*(2196), 20200131. doi: doi:10.1098/rsta.2020.0131

Abercrombie, R. E., & Rice, J. R. (2005, Aug). Can observations of earthquake scaling constrain slip weakening? *Geophys. J. Int.*, *162*(2), 406–424.

Andrews. (1985). Dynamic plane-strain shear rupture with a slip-weakening friction law calculated by a boundary integral method. *BSSA*. doi: https://doi.org/10.1785/BSSA0750010001

Aochi, H., & Twardzik, C. (2020). Imaging of seismogenic asperities of the 2016 ml 6.0 amatrice, central italy, earthquake through dynamic rupture simulations [Journal Article]. *Pure and Applied Geophysics*, *177*(5), 1931-1946. Retrieved from https://doi.org/10.1007/s00024-019-02199-z doi: 10.1007/s00024-019-02199-z

Audet, P., Bostock, M. G., Christensen, N. I., & Peacock, S. M. (2009, Jan). Seismic evidence for overpressured subducted oceanic crust and megathrust fault sealing. *Nature*, *457*, 76–78. doi: 10.1038/nature07650

Audet, P., & Burgmann, R. (2014, Jun). Possible control of subduction zone slow-earthquake periodicity by silica enrichment. *Nature*, *510*, 389–393. doi: 10.1038/nature13391

Beeler, N. M., Tullis, T. E., Blanpied, M. L., & Weeks, J. D. (1996, Apr). Frictional behavior of large displacement experimental faults. *J. Geophys. Res.*, *101*(B4), 8697–8715.

Bilek, S. L., & Lay, T. (1999). Rigidity variations with depth along interplate megathrust faults in subduction zones. *Nature*, *400*(6743), 443-446. doi: 10.1038/22739

Breuer, A., Heinecke, A., Rettenberger, S., Bader, M., Gabriel, A.-A., & Pelties, C. (2014). Sustained petascale performance of seismic simulations with seissol on supermuc. In *International supercomputing conference* (pp. 1–18).

Byerlee, J. (1978). Friction of rocks [Book Section]. In *Rock friction and earthquake prediction* (p. 615-626). Springer.

Bürgmann, R. (2018). The geophysics, geology and mechanics of slow fault slip. *Earth Planet. Sci. Lett.*, *495*, 112-134. doi: https://doi.org/10.1016/j.epsl.2018.04.062

Collettini, C., Tesei, T., Scuderi, M., Carpenter, B., & Viti, C. (2019). Beyond byerlee friction, weak faults and implications for slip behavior. *Earth and Planetary Science Letters*, *519*, 245-263. Retrieved from https://www.sciencedirect.com/science/article/pii/

S0012821X19302791 doi: https://doi.org/10.1016/j.epsl.2019.05.011

Day, S. M. (1982). Three-dimensional simulation of spontaneous rupture: the effect of nonuniform prestress. *Bulletin of the Seismological Society of America*, *72*(6A), 1881–1902.

Day, S. M., Dalguer, L. A., Lapusta, N., & Liu, Y. (2005). Comparison of finite difference and boundary integral solutions to three-dimensional spontaneous rupture. *J. Geophys. Res.*, *110*(B12). doi: 10.1029/2005jb003813

DeMets, C., Gordon, R. G., & Argus, D. F. (2010). Geologically current plate motions. *Geophys. J. Int.*, *181*(1), 1-80. doi: 10.1111/j.1365-246X.2009.04491.x

Dieterich, J. H. (1979). Modeling of rock friction 1. Experimental results and constitutive equations. *J. Geophys. Res*, *84*(B5), 2161–2168. doi: 10.1029/JB084iB05p02161

Di Toro, G., Goldsby, D. L., & Tullis, T. E. (2004). Friction falls towards zero in quartz rock as slip velocity approaches seismic rates. *Nature*, *427*(6973), 436-439. doi: 10.1038/nature02249

Dougherty, S. L., & Clayton, R. W. (2014). Seismicity and structure in central mexico: Evidence for a possible slab tear in the south cocos plate [Journal Article]. *J. Geophys. Res.*, *119*(4), 3424-3447. Retrieved from https://agupubs.onlinelibrary.wiley.com/doi/abs/10.1002/2013JB010883 doi: 10.1002/2013jb010883

Douglas, A., Beavan, J., Wallace, L., & Townend, J. (2005, Aug). Slow slip on the northern Hikurangi subduction interface, New Zealand. *Geophys. Res. Lett.*, *32*(L16305). doi: 10.1029/2005GL023607

Dragert, H., Wang, K., & James, T. S. (2001, May). A silent slip event on the deeper Cascadia subduction interface. *Science*, *292*(5521), 1525–1528. doi: 10.1126/science.1060152

Dumbser, M., & Käser, M. (2006). An arbitrary high-order discontinuous galerkin method for elastic waves on unstructured meshes - ii. the three-dimensional isotropic case [Journal Article]. *Geophys. J. Int.*, *167*(1), 319-336. Retrieved from https://onlinelibrary.wiley.com/doi/abs/10.1111/j.1365-246X.2006.03120.x doi: 10.1111/j.1365-246X.2006.03120.x

Dziewonski, A. M., Chou, T.-A., & Woodhouse, J. H. (1981). Determination of earthquake source parameters from waveform data for studies of global and regional seismicity. *Journal of Geophysical Research: Solid Earth*, *86*(B4), 2825-2852. doi: https://doi.org/10.1029/JB086iB04p02825

Ekström, G., Nettles, M., & Dziewoński, A. (2012). The global cmt project 2004–2010: Centroid-moment tensors for 13,017 earthquakes. *Physics of the Earth and Planetary Interiors*, *200*, 1–9.

Erickson, B. A., Jiang, J., Lambert, V., Barbot, S. D., Abdelmeguid, M., Almquist, M., ... Yang, Y. (2023). Incorporating full elastodynamic effects and dipping fault geometries in community code verification exercises for simulations of earthquake sequences and aseismic slip (seas). *Bull. Seismol. Soc. Am.*. doi: 10.1785/0120220066

Frank, W., Shapiro, N., Husker, A., Kostoglodov, V., Bhat, H., & Campillo, M. (2015). Along-fault pore-pressure evolution during a slow-slip event in guerrero, mexico. *Earth and Planetary Science Letters*, *413*, 135–143. doi: http://dx.doi.org/10.1016/j.epsl.2014.12.051

Frank, W. B., Radiguet, M., Rousset, B., Shapiro, N. M., Husker, A. L., Kostoglodov, V., ... Campillo, M. (2015). Uncovering the geodetic signature of silent slip through repeating earthquakes [Journal Article]. *Geophys. Res. Lett.*, 2774–2779. doi: 10.1002/2015gl063685

Gabriel, A.-A., Ampuero, J.-P., Dalguer, L. A., & Mai, P. M. (2012). The transition of dynamic rupture styles in elastic media under velocity-weakening friction. *J. Geophys. Res.*, *117*(B9). doi: doi:10.1029/2012JB009468

Galis, M., Pelties, C., Kristek, J., Moczo, P., Ampuero, J.-P., & Mai, P. M. (2014, 12). On the initiation of sustained slip-weakening ruptures by localized stresses. *Geophysical Journal International*, *200*(2), 890-909. doi: 10.1093/gji/ggu436

Gallovic, F., Valentová, Ĺ., Ampuero, J.-P., & Gabriel, A.-A. (2019). Bayesian dynamic finite-fault inversion: 2. application to the 2016 mw 6.2 amatrice, italy, earthquake [Journal Article]. *Journal of Geophysical Research: Solid Earth*, *124*(7), 6970-6988. Retrieved from https://agupubs.onlinelibrary.wiley.com/doi/abs/10.1029/2019JB017512 doi: https://doi.org/10.1029/2019JB017512

Galvez, P., Ampuero, J.-P., Dalguer, L. A., Somala, S. N., & Nissen-Meyer, T. (2014). Dynamic earthquake rupture modelled with an unstructured 3-d spectral element method applied to the 2011 m 9 tohoku earthquake. *Geophysical Journal International*, *198*(2), 1222–1240.

Galvez, P., Dalguer, L. A., Ampuero, J., & Giardini, D. (2016). Rupture reactivation during the 2011 mw 9.0 tohoku earthquake: Dynamic rupture and ground-motion simulationsrupture reactivation during the 2011 mw 9.0 tohoku earthquake: Dynamic rupture and ground-motion simulations. *Bull. Seismol. Soc. Am.*, *106*(3), 819-831. doi: 10.1785/0120150153

Gao, X., & Wang, K. (2017). Rheological separation of the megathrust seismogenic zone and

episodic tremor and slip. *Nature*.

Gualandi, A., Perfettini, H., Radiguet, M., Cotte, N., & Kostoglodov, V. (2017a). Gps deformation related to the mw 7.3, 2014, papanoa earthquake (mexico) reveals the aseismic behavior of the guerrero seismic gap. *Geophysical Research Letters*, *44*(12), 6039–6047.

Gualandi, A., Perfettini, H., Radiguet, M., Cotte, N., & Kostoglodov, V. (2017b). Gps deformation related to the mw 7.3, 2014, papanoa earthquake (mexico) reveals the aseismic behavior of the guerrero seismic gap. *Geophys. Res. Lett.*, *44*(12), 6039-6047. doi: 10.1002/2017gl072913

Guatteri, M., & Spudich, P. (2000). What can strong-motion data tell us about slip-weakening fault-friction laws? *Bulletin of the Seismological Society of America*, *90*(1), 98–116.

Harris, R. A., Barall, M., Aagaard, B. T., Ma, S., & Daniel Roten, e. a., Kim B. Olsen. (2018). A suite of exercises for verifying dynamic earthquake rupture codes. *Seismol. Res. Lett.*, *89*(3), 1146-1162. doi: 10.1785/0220170222

Harris, R. A., Barall, M., Lockner, D. A., Moore, D. E., Ponce, D. A., Graymer, R. W., ... Eberhart-Phillips, D. (2021). A geology and geodesy based model of dynamic earthquake rupture on the rodgers creek-hayward-calaveras fault system, california. *Journal of Geophysical Research: Solid Earth*, *126*(3). doi: https://doi.org/10.1029/2020JB020577

He, C., Wang, Z., & Yao, W. (2007). Frictional sliding of gabbro gouge under hydrothermal conditions. *Tectonophys.*, *445*, 353–362. doi: 10.1016/j.tecto.2007.09.008

Heinecke, A., Breuer, A., Rettenberger, S., Bader, M., Gabriel, A., Pelties, C., ... Dubey, P. (2014). Petascale high order dynamic rupture earthquake simulations on heterogeneous supercomputers [Conference Proceedings]. In *Sc '14: Proceedings of the international conference for high performance computing, networking, storage and analysis* (p. 3-14). Retrieved from https://ieeexplore.ieee.org/document/7012188/?reload=truehttps://ieeexplore.ieee.org/document/7012188/ doi: 10.1109/SC.2014.6

Hilley, G. E., Brodsky, E. E., Roman, D., Shillington, D. J., Brudzinski, M., Behn, M., ... RCN, t. S. (2022). Sz4d implementation plan. *SZ4D*. doi: https://doi.org/10.25740/hy589fc7561

Hirono, T., Tsuda, K., Tanikawa, W., Ampuero, J. P., Shibazaki, B., Kinoshita, M., & Mori, J. J. (2016). Near-trench slip potential of megaquakes evaluated from fault properties and conditions. *Scientific reports*, *6*, 28184. doi: 10.1038/srep28184

Husker, A. L., Kostoglodov, V., Cruz-Atienza, V. M., Legrand, D., Shapiro, N. M., Payero, J. S., ... Huesca-Pérez, E. (2012). Temporal variations of non-volcanic tremor (nvt)

locations in the mexican subduction zone: Finding the nvt sweet spot. *Geochemistry, Geophysics, Geosystems*, *13*(3).

Ida, Y. (1972). Cohesive force across the tip of a longitudinal-shear crack and griffith's specific surface energy. *Journal of Geophysical Research*, *77*(20), 3796–3805.

Jiang, J., Erickson, B. A., Lambert, V. R., Ampuero, J.-P., Ando, R., Barbot, S. D., ... van Dinther, Y. (2022). Community-driven code comparisons for three-dimensional dynamic modeling of sequences of earthquakes and aseismic slip. *J. Geophys. Res.*, *127*(3), e2021JB023519. doi: https://doi.org/10.1029/2021JB023519

Kaneko, Y., Fukuyama, E., & Hamling, I. J. (2017). Slip-weakening distance and energy budget inferred from near-fault ground deformation during the 2016 mw7.8 kaikoura earthquake. *Geophys. Res. Lett.*, *44*(10), 4765-4773. doi: https://doi.org/10.1002/2017GL073681

Käser, M., & Dumbser, M. (2006). An arbitrary high-order discontinuous galerkin method for elastic waves on unstructured meshes - i. the two-dimensional isotropic case with external source terms [Journal Article]. *Geophys. J. Int.*, *166*(2), 855-877. Retrieved from ⟨GotoISI⟩://WOS:000239004900027 doi: 10.1111/j.1365-246X.2006.03051.x

Kato, A., Obara, K., Igarashi, T., Tsuruoka, H., Nakagawa, S., & Hirata, N. (2012). Propagation of slow slip leading up to the 2011 mw 9.0 tohoku-oki earthquake. *Science*, *335*(6069), 705-708. doi: 10.1126/science.1215141

Kato, N. (2012). Fracture energies at the rupture nucleation points of large interplate earthquakes. *Earth and Planetary Science Letters*, *353-354*, 190-197. Retrieved from https://www.sciencedirect.com/science/article/pii/S0012821X12004426 doi: https://doi.org/10.1016/j.epsl.2012.08.015

Khoshmanesh, M., Shirzaei, M., & Uchida, N. (2020). Deep slow-slip events promote seismicity in northeastern japan megathrust [Journal Article]. *Earth Planet. Sci. Lett.*, *540*. doi: 10.1016/j.epsl.2020.116261

Kim, Y., Clayton, R. W., & Jackson, J. M. (2010). Geometry and seismic properties of the subducting cocos plate in central mexico [Journal Article]. *J. Geophys. Res.*, *115*(B6). Retrieved from https://agupubs.onlinelibrary.wiley.com/doi/abs/10.1029/2009JB006942 doi: doi:10.1029/2009JB006942

Kostoglodov, V., Bandy, W., Dominguez, J., & Mena, M. (1996). Gravity and seismicity over the Guerrero seismic gap, Mexico. *Geophys. Res. Lett*, *23*(23), 3385–3388.

Krenz, L., Uphoff, C., Ulrich, T., Gabriel, A.-A., Abrahams, L. S., Dunham, E. M., & Bader, M. (2021). 3D Acoustic-Elastic Coupling with Gravity: The Dynamics of the 2018

Palu, Sulawesi Earthquake and Tsunami. In *The International Conference for High Performance Computing, Networking, Storage and Analysis.* Association for Computing Machinery. doi: 10.1145/3458817.3476173

Lapusta, N., & Liu, Y. (2009). Three-dimensional boundary integral modeling of spontaneous earthquake sequences and aseismic slip. *J. Geophys. Res.*, *114*(B09303). doi: 10.1029/2008JB005934

Lay, T., Kanamori, H., Ammon, C. J., Koper, K. D., Hutko, A. R., Ye, L., ... Rushing, T. M. (2012). Depth-varying rupture properties of subduction zone megathrust faults. *J. Geophys. Res.*, *117*(B04311), B04311. doi: https://doi.org/10.1029/2011JB009133

Li, D., & Liu, Y. (2016). Spatiotemporal evolution of slow slip events in a non-planar fault model for northern cascadia subduction zone [Journal Article]. *Journal of Geophysical Research: Solid Earth*, *63*(3), 959–968. doi: 10.1002/2016JB012857

Li, D., & Liu, Y. (2017). Modeling slow-slip segmentation in cascadia subduction zone constrained by tremor locations and gravity anomalies. *Journal of Geophysical Research: Solid Earth*, n/a–n/a. Retrieved from http://dx.doi.org/10.1002/2016JB013778 (2016JB013778) doi: 10.1002/2016JB013778

Linde, A. T., Gladwin, M. T., Johnston, M. J., Gwyther, R. L., & Bilham, R. G. (1996). A slow earthquake sequence on the san andreas fault. *Nature*, *383*(6595), 65.

Liu, Y., & Rice, J. R. (2007, Sep). Spontaneous and triggered aseismic deformation transients in a subduction fault model. *J. Geophys. Res.*, *112*(B09404). doi: 10.1029/2007JB004930

Liu, Y., & Rice, J. R. (2009, Sep). Slow slip predictions based on granite and gabbro friction data compared to GPS measurements in northern Cascadia. *J. Geophys. Res.*, *114*(B09407). doi: 10.1029/2008JB006142

Lowry, A. R., Larson, K. M., Kostoglodov, V., & Bilham, R. (2001, Oct). Transient fault slip in Guerrero, southern Mexico. *Geophys. Res. Lett.*, *28*(19), 3753–3756.

Madden, E. H., Ulrich, T., & Gabriel, A.-A. (2022). The state of pore fluid pressure and 3-d megathrust earthquake dynamics. *J. Geophys. Res.*, *127*(4), e2021JB023382. doi: https://doi.org/10.1029/2021JB023382

Manea, V. C., & Manea, M. (2011). Flat-slab thermal structure and evolution beneath central mexico. *Pure and Applied Geophysics*, *168*(8), 1475-1487. doi: 10.1007/s00024-010-0207-9

Marone, C. (1998). Laboratory-derived friction laws and their application to seismic faulting.

*Annual Review of Earth and Planetary Sciences*, *26*(1), 643–696.

Meng, Q., & Duan, B. (2022). Dynamic modeling of interactions between shallow slow-slip events and subduction earthquakes. *Seismol. Res. Lett.*. doi: 10.1785/0220220138

Mikumo, T., Olsen, K. B., Fukuyama, E., & Yagi, Y. (2003). Stress-breakdown time and slip-weakening distance inferred from slip-velocity functions on earthquake faults. *Bull. Seismol. Soc. Am.*, *93*(1), 264-282. doi: 10.1785/0120020082

Noda, H., Dunham, E. M., & Rice, J. R. (2009). Earthquake ruptures with thermal weakening and the operation of major faults at low overall stress levels. *J. Geophys. Res.*, *114*(B07302). doi: 10.1029/2008JB006143

Noda, H., Lapusta, N., & Kanamori, H. (2013). Comparison of average stress drop measures for ruptures with heterogeneous stress change and implications for earthquake physics. *Geophys. J. Int.*, *193*(3), 1691-1712. doi: 10.1093/gji/ggt074

Obara, K., & Kato, A. (2016). Connecting slow earthquakes to huge earthquakes. *Science*, *353*(6296), 253–257.

Oeser, J., Bunge, H.-P., & Mohr, M. (2006). Cluster design in the earth sciences tethys. In *International conference on high performance computing and communications* (pp. 31–40).

Oglesby, D. D., & Mai, P. M. (2012). Fault geometry, rupture dynamics and ground motion from potential earthquakes on the north anatolian fault under the sea of marmara. *Geophysical Journal International*, *188*(3), 1071-1087. doi: https://doi.org/10.1111/j.1365-246X.2011.05289.x

Palmer, A. C., & Rice, J. R. (1973). The growth of slip surfaces in the progressive failure of over-consolidated clay. *Proceedings of the Royal Society of London. A. Mathematical and Physical Sciences*, *332*(1591), 527-548.

Pelties, C., de la Puente, J., Ampuero, J.-P., Brietzke, G. B., & Käser, M. (2012). Three-dimensional dynamic rupture simulation with a high-order discontinuous galerkin method on unstructured tetrahedral meshes [Journal Article]. *J. Geophys. Res.*, *117*(B2). Retrieved from https://agupubs.onlinelibrary.wiley.com/doi/abs/10.1029/2011JB008857 doi: doi:10.1029/2011JB008857

Pelties, C., Gabriel, A. A., & Ampuero, J. P. (2014). Verification of an ader-dg method for complex dynamic rupture problems [Journal Article]. *Geosci. Model Dev.*, *7*(3), 847-866. Retrieved from https://www.geosci-model-dev.net/7/847/2014/ doi: 10.5194/gmd-7-847-2014

Peng, Z., & Gomberg, J. (2010, Sep). An integrated perspective of the continuum between

earthquakes and slow-slip phenomena. *Nature Geoscience*, *3*, 599–607. doi: 10.1038/ngeo940

Perez-Silva, A., Li, D., Gabriel, A.-A., & Kaneko, Y. (2021). 3d modeling of long-term slow slip events along the flat-slab segment in the guerrero seismic gap, mexico. *Geophys. Res. Lett.*, *48*(13), e2021GL092968. doi: https://doi.org/10.1029/2021GL092968

Perry, S. M., Lambert, V., & Lapusta, N. (2020). Nearly magnitude-invariant stress drops in simulated crack-like earthquake sequences on rate-and-state faults with thermal pressurization of pore fluids. *J. Geophys. Res.*, *125*(3), e2019JB018597. doi: https://doi.org/10.1029/2019JB018597

Plata-Martinez, R., Ide, S., Shinohara, M., Garcia, E. S., Mizuno, N., Dominguez, L. A., ... Ito, Y. (2021). Shallow slow earthquakes to decipher future catastrophic earthquakes in the guerrero seismic gap. *Nature communications*, *12*(1), 3976. doi: 10.1038/s41467-021-24210-9

Pritchard, M. E., Allen, R. M., Becker, T. W., Behn, M. D., Brodsky, E. E., Bürgmann, R., ... Vincent, H. (2020). New opportunities to study earthquake precursors [Journal Article]. *Seismol. Res. Lett.*, *91*(5), 2444-2447. Retrieved from https://doi.org/10.1785/0220200089 doi: 10.1785/0220200089

Pérez-Campos, X., Kim, Y., Husker, A., Davis, P. M., Clayton, R. W., Iglesias, A., ... Gurnis, M. (2008). Horizontal subduction and truncation of the cocos plate beneath central mexico. *Geophys. Res. Lett.*, *35*(18). doi: doi:10.1029/2008GL035127

Radiguet, M., Cotton, F., Vergnolle, M., Campillo, M., Walpersdorf, A., Cotte, N., & Kostoglodov, V. (2012). Slow slip events and strain accumulation in the guerrero gap, mexico. *Journal of Geophysical Research: Solid Earth*, *117*(B4). Retrieved from http://dx.doi.org/10.1029/2011JB008801 doi: 10.1029/2011JB008801

Radiguet, M., Perfettini, H., Cotte, N., Gualandi, A., Valette, B., Kostoglodov, V., ... Campillo, M. (2016). Triggering of the 2014 mw7.3 papanoa earthquake by a slow slip event in guerrero, mexico [Journal Article]. *Nature Geosci*. Retrieved from http://dx.doi.org/10.1038/ngeo2817 doi: 10.1038/ngeo2817

Ramos, M. D., & Huang, Y. (2019). How the transition region along the cascadia megathrust influences coseismic behavior: Insights from 2-d dynamic rupture simulations. *Geophys. Res. Lett.*, *46*(4), 1973-1983.

Ramos, M. D., Huang, Y., Ulrich, T., Li, D., Gabriel, A.-A., & Thomas, A. M. (2021). Assessing margin-wide rupture behaviors along the cascadia megathrust with 3-d dynamic

rupture simulations. *J. Geophys. Res.*, *126*(7), e2021JB022005. doi: https://doi.org/10.1029/2021JB022005

Rettenberger, S., Meister, O., Bader, M., & Gabriel, A.-A. (2016). Asagi: A parallel server for adaptive geoinformation. In *Proceedings of the exascale applications and software conference 2016*. New York, NY, USA: Association for Computing Machinery. Retrieved from https://doi.org/10.1145/2938615.2938618 doi: 10.1145/2938615.2938618

Rice, J. R. (1993, Jun). Spatiotemporal complexity of slip on a fault. *J. Geophys. Res.*, *98*(B6), 9885–9907. doi: 10.1029/93JB00191

Rice, J. R., & Ben-Zion, Y. (1996, Apr). Slip complexity in earthquake fault models. *Proc. Natl. Acad. Sci.*, *93*(9), 3811–3818.

Rousset, B., Bürgmann, R., & Campillo, M. (2019). Slow slip events in the roots of the san andreas fault [Journal Article]. *Science Advances*, *5*(2), eaav3274. Retrieved from http://advances.sciencemag.org/content/5/2/eaav3274.abstract doi: 10.1126/sciadv.aav3274

Rubin, A. M., & Ampuero, J.-P. (2005). Earthquake nucleation on (agine) rate and state faults. *J. Geophys. Res.*, *110*(B11312). doi: 10.1029/2005JB003686

Ruina, A. L. (1983). Slip instability and state variable friction laws. *J. Geophys. Res.*, *88*(B12), 10359–10370. doi: 10.1029/JB088iB12p10359

Ruiz, S., Metois, M., Fuenzalida, A., Ruiz, J., Leyton, F., Grandin, R., ... Campos, J. (2014). Intense foreshocks and a slow slip event preceded the 2014 iquique mw8.1 earthquake [Journal Article]. *Science*, *345*, 1165-1169. doi: 10.1126/science.1256074

Saffer, D. M., & Wallace, L. M. (2015). The frictional, hydrologic, metamorphic and thermal habitat of shallow slow earthquakes. *Nature Geoscience*, *8*(8), 594-600. doi: 10.1038/ngeo2490

Schwartz, S. Y., & Rokosky, J. M. (2007). Slow slip events and seismic tremor at circum-Pacific subduction zones. *Reviews of Geophysics*, *45*. doi: 10.1029/2006RG000208.

Shelly, D. R., Beroza, G. C., & Ide, S. (2007, Mar). Non-volcanic tremor and low-frequency earthquake swarms. *Nature*. doi: 10.1038/nature05666

Shelly, D. R., Beroza, G. C., Ide, S., & Nakamula, S. (2006, Jul). Low-frequency earthquakes in Shikoku, Japan, and their relationship to episodic tremor and slip. *Nature*, *442*(7099), 188–191. doi: 10.1038/nature04931

Socquet, A., Valdes, J. P., Jara, J., Cotton, F., Walpersdorf, A., Cotte, N., ... Norabuena, E. (2017a). An 8 month slow slip event triggers progressive nucleation of the 2014 chile megathrust [Journal Article]. *Geophys. Res. Lett.*, *44*(9), 4046-4053. Retrieved from

https://agupubs.onlinelibrary.wiley.com/doi/abs/10.1002/2017GL073023https://agupubs.onlinelibrary.wiley.com/doi/full/10.1002/2017GL073023 doi: 10.1002/2017gl073023

Socquet, A., Valdes, J. P., Jara, J., Cotton, F., Walpersdorf, A., Cotte, N., ... Norabuena, E. (2017b). An 8 month slow slip event triggers progressive nucleation of the 2014 chile megathrust. *Geophys. Res. Lett.*, *44*(9), 4046-4053. doi: 10.1002/2017gl073023

Song, T. R., Helmberger, D. V., Brudzinski, M. R., Clayton, R. W., Davis, P., Perez-Campos, X., & Singh, S. K. (2009). Subducting slab ultra-slow velocity layer coincident with silent earthquakes in southern mexico [Journal Article]. *Science*, *324*(5926), 502-6. Retrieved from http://www.ncbi.nlm.nih.gov/pubmed/19390043http://www.sciencemag.org/content/324/5926/502.full.pdf doi: 10.1126/science.1167595

Stuart, W. D., Hildenbrand, T. G., & Simpson, R. W. (1997, Dec). Stressing of the New Madrid Seismic Zone by a lower crust detachment fault. *J. Geophys. Res.*, *102*(B12). doi: 10.1029/97jb02716

Thomas, M. Y., Lapusta, N., Noda, H., & Avouac, J.-P. (2014). Quasi-dynamic versus fully dynamic simulations of earthquakes and aseismic slip with and without enhanced coseismic weakening. *Journal of Geophysical Research: Solid Earth*, *119*(3), 1986-2004. Retrieved from https://agupubs.onlinelibrary.wiley.com/doi/abs/10.1002/2013JB010615 doi: https://doi.org/10.1002/2013JB010615

Tinti, E., Casarotti, E., Ulrich, T., Taufiqurrahman, T., Li, D., & Gabriel, A.-A. (2021). Constraining families of dynamic models using geological, geodetic and strong ground motion data: The mw 6.5, october 30th, 2016, norcia earthquake, italy. *Earth Planet. Sci. Lett.*, *576*. doi: 10.1016/j.epsl.2021.117237

Tinti, E., Spudich, P., & Cocco, M. (2005). Earthquake fracture energy inferred from kinematic rupture models on extended faults. *J. Geophys. Res.*, *110*(B12). doi: 10.1029/2005jb003644

Tobin, H. J., & Saffer, D. M. (2009). Elevated fluid pressure and extreme mechanical weakness of a plate boundary thrust, nankai trough subduction zone [Journal Article]. *Geology*, *37*(8), 679-682.

Uchida, N., & Bürgmann, R. (2021). A decade of lessons learned from the 2011 tohoku-oki earthquake. *Reviews of Geophysics*, *59*(2). doi: https://doi.org/10.1029/2020RG000713

Uchida, N., Iinuma, T., Nadeau, R. M., Bürgmann, R., & Hino, R. (2016). Periodic slow slip triggers megathrust zone earthquakes in northeastern japan. *Science*, *351*(6272), 488-492. doi: doi:10.1126/science.aad3108

Ulrich, T., Gabriel, A.-A., & Madden, E. H. (2022). Stress, rigidity and sediment strength control megathrust earthquake and tsunami dynamics. *Nature Geosci.*, *15*(1), 67-73. doi: 10.1038/s41561-021-00863-5

Uphoff, C., May, D. A., & Gabriel, A.-A. (2023). A discontinuous galerkin method for sequences of earthquakes and aseismic slip on multiple faults using unstructured curvilinear grids. *Geophysical Journal International*, *233*(1), 586–626.

Uphoff, C., Rettenberger, S., Bader, M., Madden, E. H., Ulrich, T., Wollherr, S., & Gabriel, A.-A. (2017). *Extreme scale multi-physics simulations of the tsunamigenic 2004 sumatra megathrust earthquake* [Conference Paper]. doi: 10.1145/3126908.3126948

Vallee, M., Charléty, J., Ferreira, A. M. G., Delouis, B., & Vergoz, J. (2011). Scardec: a new technique for the rapid determination of seismic moment magnitude, focal mechanism and source time functions for large earthquakes using body-wave deconvolution. *Geophys. J. Int.*, *184*(1), 338-358. doi: 10.1111/j.1365-246X.2010.04836.x

van Zelst, I., Wollherr, S., Gabriel, A.-A., Madden, E. H., & van Dinther, Y. (2019). Modeling megathrust earthquakes across scales: One-way coupling from geodynamics and seismic cycles to dynamic rupture [Journal Article]. *Journal of Geophysical Research: Solid Earth*, *124*(11), 11414-11446. Retrieved from https://agupubs.onlinelibrary.wiley.com/doi/abs/10.1029/2019JB017539 doi: https://doi.org/10.1029/2019JB017539

Walton, M. A., Staisch, L. M., Dura, T., Pearl, J. K., Sherrod, B., Gomberg, J., ... Wirth, E. (2021). Toward an integrative geological and geophysical view of cascadia subduction zone earthquakes. *Annual Review of Earth and Planetary Sciences*, *49*(1), 367-398. doi: 10.1146/annurev-earth-071620-065605

Wang, K. (2010). Finding fault in fault zones. *Science*, *329*(5988), 152-153. doi: 10.1126/science.1192223

Wollherr, S., Gabriel, A.-A., & Mai, P. M. (2019). Landers 1992 "reloaded": Integrative dynamic earthquake rupture modeling. *J. Geophys. Res.*, *124*(7), 6666-6702. doi: https://doi.org/10.1029/2018JB016355

Wollherr, S., Gabriel, A.-A., & Uphoff, C. (2018). Off-fault plasticity in three-dimensional dynamic rupture simulations using a modal discontinuous galerkin method on unstructured meshes: implementation, verification and application [Journal Article]. *Geophys. J. Int.*, *214*(3), 1556-1584. Retrieved from https://doi.org/10.1093/gji/ggy213 doi: 10.1093/gji/ggy213

Ye, L., Lay, T., Kanamori, H., & Rivera, L. (2016). Rupture characteristics of major and great

($m_w \leq 7.0$) megathrust earthquakes from 1990 to 2015: 2.depth dependence. *J. Geophys. Res.*, *121*(2), 845-863. doi: 10.1002/2015jb012427

Zhu, W., Allison, K. L., Dunham, E. M., & Yang, Y. (2020). Fault valving and pore pressure evolution in simulations of earthquake sequences and aseismic slip. *Nature communications*, *11*(1), 4833. doi: 10.1038/s41467-020-18598-z